JGR Oceans

RESEARCH ARTICLE
10.1029/2019JC015639

Circulation and Thermohaline Variability of the Hanna Shoal Region on the Northeastern Chukchi Sea Shelf

Ying-Chih Fang[1,2], Thomas J. Weingartner[2], Elizabeth L. Dobbins[2], Peter Winsor[2,3], Hank Statscewich[2], Rachel A. Potter[2], Todd D. Mudge[4], Chase A. Stoudt[2,5], and Keath Borg[4]

[1]Alfred Wegener Institute, Helmholtz Centre for Polar and Marine Research, Bremerhaven, Germany, [2]College of Fisheries and Ocean Sciences, University of Alaska Fairbanks, Fairbanks, Alaska, United States, [3]WWF Arctic Programme, WWF-Canada, Ottawa, Ontario, Canada, [4]ASL Environmental Sciences, Inc., Victoria, British Columbia, Canada, [5]Bureau of Ocean Energy Management, U.S. Department of the Interior, Anchorage, Alaska, United States

Key Points:
- Stratification on the eastern side of Hanna Shoal is maintained year-round, unlike other locations on the northeastern Chukchi shelf
- Baroclinic flows driven by winter-evolved along-isobath density gradients are pronounced in winter on the eastern side of Hanna Shoal
- A coherent signal with a ~3-day period circulating Hanna Shoal is described, with features consistent to a barotropic topographic wave

Correspondence to:
Y.-C. Fang,
ying-chih.fang@awi.de

Citation:
Fang, Y.-C., Weingartner, T. J., Dobbins, E. L., Winsor, P., Statscewich, H., Potter, R. A., et al. (2020). Circulation and thermohaline variability of the Hanna Shoal region on the northeastern Chukchi Sea shelf. *Journal of Geophysical Research: Oceans*, *125*, e2019JC015639. https://doi.org/10.1029/2019JC015639

Received 10 SEP 2019
Accepted 1 JUN 2020
Accepted article online 4 JUN 2020

Abstract We analyzed velocity and hydrographic data from 23 moorings in the northeast Chukchi Sea from 2011 to 2014. In most years the eastern side of Hanna Shoal was strongly stratified year-round, while weakly stratified regions prevailed on the shelf south and west of the Shoal. Stratification differences cause differential vertical mixing rates, which in conjunction with advection of different bottom water properties resulted in seasonally varying along-isobath density gradients. In agreement with numerical models, we find that bottom waters flow anticyclonically around the Shoal. Whereas most of the shelf responded barotropically to wind-forcing, there was a strong baroclinic component to the flow field northeast of Hanna Shoal, resulting in no net vertically integrated transport on average. In contrast there is a net eastward transport from west of the Shoal, which implies convergence north of the Shoal. Convergence and along-isobath density gradients may foster cross-shelf exchange north of Hanna Shoal. Modal analyses indicate that the shelf south of the Shoal and Barrow Canyon responded coherently to local and remote winds, whereas the wind-current response around Hanna Shoal was less coherent. Barotropic topographic waves, of ~3-day period, were generated episodically northeast of the Shoal and propagate clockwise around Hanna Shoal, but are blocked from entering Barrow Canyon and are possibly scattered by the horizontally sheared flow and converging isobaths on the western side of the Shoal. Analysis of water properties on the western side of Hanna Shoal suggests that these include contributions from the western and southern portions of the Chukchi Sea.

Plain Language Summary We use multiyear mooring measurements of velocity and hydrography to elucidate the circulation in the Hanna Shoal region on the northern Chukchi shelf. Hanna Shoal is a biological hot spot but has only recently received attention due to historically heavy summer sea ice cover. We find that on the eastern side of Hanna Shoal the water column is perpetually stratified and currents are strongly sheared in contrast to other locations in the northeastern Chukchi Sea. Our results imply that the shelf north of Hanna Shoal may be a site for water mass exchange between the shelf and shelfbreak. This topic deserves further study in order to determine the pathways by which Pacific and Arctic Ocean waters interact.

1. Introduction

The Chukchi Sea shelf, one of the most productive areas of the global ocean (Grebmeier et al., 2006), consists of a rich benthic ecosystem (Blanchard et al., 2017) that supports large numbers of marine mammals (Clarke et al., 1989; Grebmeier et al., 2015; Moore & Huntington, 2008; Schonberg et al., 2014). This production is sustained by the northward inflow through Bering Strait of nutrient-rich Pacific Water (PW) that is driven by the pressure gradient force between the Pacific and Arctic Oceans (Aagaard et al., 2006; Peacock & Laxon, 2004; Stigebrandt, 1984). The transport through Bering Strait, estimated to be ~1.1 Sv (Woodgate et al., 2012) and increasing at a rate of ~0.01 Sv per year (Woodgate, 2018), contributes substantial amounts of freshwater and heat that impact the shelf hydrography (e.g., Weingartner et al., 2013), sea ice cover (e.g., Shimada et al., 2006; Wood et al., 2015; Woodgate et al., 2010), and the cold Arctic halocline (e.g., Aagaard et al., 1981; Shimada et al., 2005).

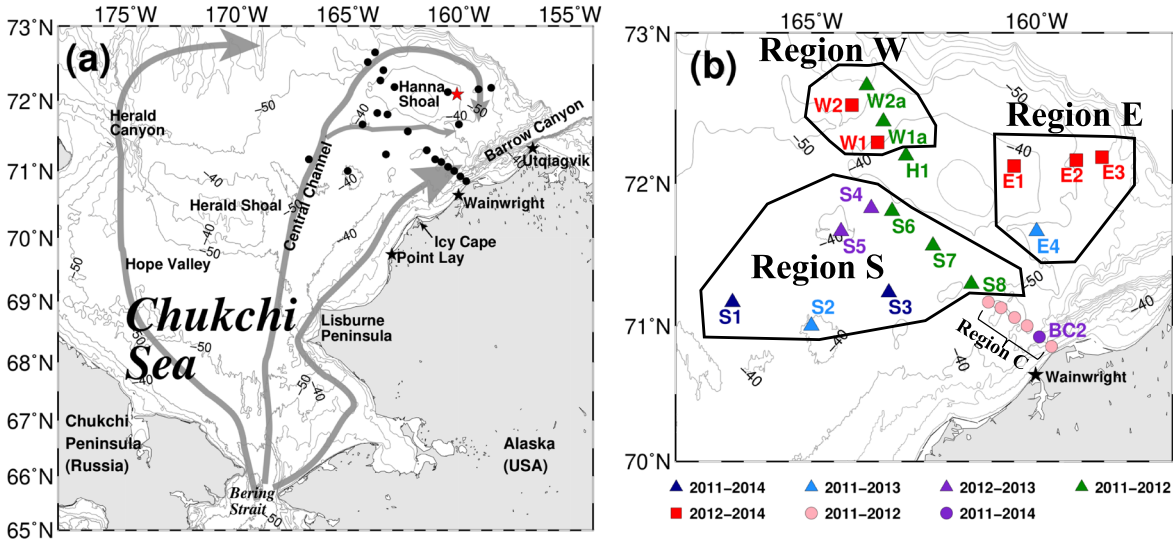

Figure 1. (a) Map of the Chukchi Sea with place names. Black dots indicate mooring sites. The red star denotes the NARR wind grid point representative of the regional winds. Black stars denote villages along the Alaskan coast. Gray arrows show schematic pathways of Pacific waters. Bathymetric contours are at 10-m intervals between 10 and 100 m. (b) Enlargement of the Hanna Shoal region and mooring sites categorized by the deployment years and projects. Triangles denote the ASL moorings, circles denote the BC moorings (BC1–BC6, with BC1 closest to the coast), and red squares indicate the COMIDA moorings. Colors denote different temporal coverages. Various moorings except H1 are grouped into regions denoting west (W moorings, region W) and east (E moorings, region E) of Hanna Shoal, southern shelf (S moorings, region S), and Barrow canyon (BC moorings, region C).

The PW throughflow on the shelf is bathymetrically steered along three major pathways (Figure 1a) as inferred from in situ observations (e.g., Pickart et al., 2010, 2016; Weingartner et al., 2005; Woodgate et al., 2005) and numerical models (Spall, 2007; Winsor & Chapman, 2004). One pathway flows through Hope Valley and Herald Canyon, another flows northward through the Central Channel (Weingartner et al., 2005; Woodgate et al., 2005), and the third flows along the Alaskan coast as the Alaskan Coastal Current (Paquette & Bourke, 1974), exiting the shelf through Barrow Canyon (e.g., Aagaard & Roach, 1990; Mountain et al., 1976). Although the mean flow on the shelf is predominately poleward, the prevailing local winds are northeasterly (Weingartner et al., 2005) and can substantially modulate, and even reverse, the shelf circulation (Weingartner et al., 1998; Woodgate et al., 2005).

These various pathways eventually join the shelfbreak circulation. For example, the outflow from Herald Valley (and to some degree from Barrow Canyon) proceeds eastward as a narrow (~10 km), bottom-confined, shelfbreak jet (Corlett & Pickart, 2017), while the surface waters, consisting of derivatives from Barrow Canyon, flow westward in the Chukchi Slope Current (Corlett & Pickart, 2017; Li et al., 2019) and eastward along the Beaufort shelfbreak (Nikolopoulos et al., 2009; Pickart, 2004). In addition, frequent shelf-break upwelling events foster shelf-basin exchanges along the outer shelf (Li et al., 2019).

Our focus here is on the circulation and hydrographic conditions around Hanna Shoal (Figure 1a), which have received comparatively little attention due to the difficulty of collecting observations in a region with historically heavy ice concentrations. The Shoal, lying at the northern end of the Central Channel and ~200 km northwest of Utqiagvik (formerly Barrow), is a zonally oriented oval ~150 and ~55 km in length along its major and minor axes, respectively. It lies ~75 km south of the shelf break (~100 m isobath) and north of the broad, gently sloping central shelf of 40–45 m depth. Minimum depths atop the Shoal are ~20 m allowing deep-keeled sea ice to ground, as evidenced by the heavily scoured seabed (Grantz & Eittreim, 1979). Grounded ice and/or sluggish flow over Hanna Shoal result in the area remaining partially ice covered in summer while the rest of the shelf is relatively ice free (Fang et al., 2017; Martin & Drucker, 1997; Wood et al., 2015). Waters flowing northward through the Central Channel appear to spread eastward south of Hanna Shoal (Weingartner et al., 2005; Weingartner, Dobbins, et al., 2013), although some continues along the west side of the Shoal (Weingartner et al., 2017). Based on a short 5-day current meter record, Johnson (1989) measured northeastward currents northwest of Hanna Shoal as did Gong and Pickart (2015) during a month-long shipboard survey. In addition, Stabeno et al. (2018) observed a mean

eastward flow of ~3 cm s^{-1} along the 30-m isobath from a year-round mooring on the north side of the Shoal and observed an anticyclonic flow around the Shoal on the basis of several deep-drogued drifter trajectories. Conversely, Weingartner, Fang, et al. (2017) calculated a swift (~10 cm s^{-1}) northwestward baroclinic flow along the shelf northeast of Hanna Shoal, which opposes the presumed along-isobath, barotropic shelf flow from the west. These conflicting observations indicate that the circulation around Hanna Shoal is not fully understood. Moreover, the circulation connections between the shelf north and south of the Shoal have not been explored.

Hydrographically, three major water masses are commonly found around Hanna Shoal and can be categorized as (i) cold (< −1°C) and saline (>32.5) Winter Water (WW) that is formed in winter due to sea ice formation; (ii) warm (3–5°C) and moderately salty Bering Sea Water (BSW), a mixture of Anadyr Water and central Bering shelf water north of Bering Strait (Coachman et al., 1975), advected northward through the Central Channel in summer (Gong & Pickart, 2015; Weingartner, Dobbins, et al., 2013); and (iii) cold (0–2°C) and fresh (<30) meltwaters (MW) resulting from ice melt. WW is nutrient-rich and, in summer, is found within ~20–25 m of the seabed surrounding the Shoal (Danielson et al., 2017; Weingartner, Fang, et al., 2017). In late summer and fall, the water column consists of a two-layer structure with a ~10–15 m thick surface layer of MW, underlain by a strong, but thin, pycnocline, capping WW (Fang et al., 2017; Weingartner, Fang, et al., 2017). Shelfbreak upwelling occurs year-round and can occasionally transport relatively warm (> −1.3°C), saline (>33.6) Atlantic Water onto the outer shelf (Li et al., 2019; Pickart et al., 2011) or into Barrow Canyon (Aagaard & Roach, 1990; Weingartner et al., 2005). Thus, Hanna Shoal may be a location where different water masses interact.

Herein we use mooring records from the northeastern Chukchi Sea shelf from 2011 to 2014 to examine circulation and hydrographic variability on the shelf surrounding Hanna Shoal. We will show that the eastern side of Hanna Shoal differs substantially from other shelf regions with respect to stratification and flow structure on annual, seasonal, and synoptic time scales. The paper is organized as follows. Data and methods are described in section 2. Section 3 begins by characterizing the regional winds and mean circulation patterns under strong northeasterly and weak winds. These results are followed by briefly investigating flow variability on the semidiurnal, and primarily on the synoptic (~3 days) and low-frequency (>8 days) time scales. Both hydrographic variability as well as the continuity of the anticyclonic transport around Hanna Shoal are also explored. Section 4 includes a summary and discusses the implication of the inferred flow convergence and potential for cross-shelf exchange north of Hanna Shoal.

2. Data and Methods

2.1. Moorings

Three separate programs supported a total of 23 current meter moorings (Figure 1b). The programs include data processed by ASL Environmental Sciences (ASL), and the Barrow Canyon (BC), and Chukchi Sea Offshore Monitoring in Drilling Area (COMIDA) programs. Although the moorings have variable record lengths, they were deployed annually from August 2011 to September 2014. In general, each mooring was equipped with a Teledyne RDI 300 or 600 kHz upward-looking ADCP mounted ~3 m above the sea floor, with vertical coverage ranging from near-bottom to ~5 m below the surface. Temporal and vertical resolutions of the current velocities for the BC and COMIDA moorings were 15–60 min and 1 m, respectively. For the ASL moorings the temporal resolution was also 15 min, but currents were only processed and archived at three depths: near-bottom, middepth, and near-surface. Data acquisition procedures for the ASL moorings are given by Mudge et al. (2015); the COMIDA and BC moorings are documented in Weingartner et al. (2016) and Weingartner et al. (2017), respectively. Mooring configurations, locations, recording periods, and vertical coverage are summarized in Table 1 and are segregated into three time periods: 2011–2012, 2012–2013, and 2013–2014. The observations are largely described in terms of their locations relative to Hanna Shoal (see Figure 1b). In this scheme, W1, W2, W1a, and W2a are west of Hanna Shoal (Region W); E1, E2, E3, and E4 are east of Hanna Shoal (Region E); the ASL S1–S8 moorings are distributed over the shelf south of the Shoal (Region S). H1 is not included because it was atop the Shoal. The BC moorings are near or in Barrow Canyon (Region C).

Data gaps in the velocity time series were random and generally less than ~3 hr in duration. Gap-free data were retrieved at depths deeper than ~15 m, but sporadic gaps totaling ~2–8% of the record length were

Table 1
Summary of Mooring Configurations

Name	Group	Lat(°W)	Lon(°N)	Bottom depth (m)	Instrument	Name	ADCP range[a] (m)	ADCP period of record (mm/dd)	CTD depth (m)	Original name[b]
2011–2012 period										
S1	ASL	166.75	71.17	46	ADCP	S1	S/20/36	7/26 to 8/9	44	Crackerjack
S2	ASL	165.00	71.00	37	ADCP	S2	S/15/27	7/28 to 8/12	31	CPAI01
S3	ASL	163.28	71.24	45	ADCP	S3	S/17/35	8/2 to 8/12	N/A	Burger
S6	ASL	163.21	71.81	43	ADCP	S6	S/18/30	8/28 to 8/4	N/A	H04
S7	ASL	162.30	71.57	45	ADCP	S7	S/18/32	8/27 to 7/22	N/A	H05
S8	ASL	161.45	71.30	49	ADCP	S8	S/20/36	8/27 to 6/14	N/A	H06
W1a	ASL	163.40	72.42	42	ADCP	W1a	S/19/33	8/28 to 7/9	N/A	H02
W2a	ASL	163.77	72.66	58	ADCP	W2a	S/25/45	8/28 to 8/9	N/A	H01
H1	ASL	162.90	72.19	40	ADCP	H1	S/15/27	8/28 to 7/4	N/A	H03
E4	ASL	160.00	71.67	45	ADCP	E2	S/23/41	8/3 to 8/24	43	CPAI02
BC1	BC	159.67	70.85	30	ADCP/TCP	BC1	4–26	8/30 to 7/7	31	BC1
BC2	BC	159.94	70.92	52	ADCP/TCP	BC2	12–46	8/30 to 5/4	49	BC2
BC3	BC	160.21	71.00	53	ADCP/TCP	BC3	10–46	8/30 to 7/4	49	BC3
BC4	BC	160.49	71.06	49	ADCP/TCP	BC4	11–42	8/30 to 7/19	45	BC4
BC5	BC	160.79	71.13	50	ADCP/TCP	BC5	12–42	8/30 to 5/3	46	BC5
BC6	BC	161.07	71.17	47	ADCP/TCP	BC6	5–40	8/30 to 10/31 (in 2011)	43	BC6
2012–2013 period										
S1	ASL	166.75	71.17	46	ADCP/TC	S1	S/20/36	08/9 to 7/31	44	Crackerjack
S2	ASL	165.00	71.00	37	ADCP/TC	S2	S/17/27	8/13 to 7/31	31	CPAI01
S3	ASL	163.28	71.24	45	ADCP/TC	S3	S/16/34	8/12 to 7/31	45	Burger
S4	ASL	163.67	71.83	44	ADCP/TC	S4	S/17/31	8/10 to 8/1	36	Statoil3
S5	ASL	164.34	71.67	38	ADCP/TC	S5	S/15/25	8/16 to 9/2	31	Statoil4
W1	COMIDA	163.53	72.28	41	ADCP/TCP	W1	9–36	8/16 to 9/9	36	NW40
W2	COMIDA	164.10	72.53	50	ADCP/TCP	W2	24–46	8/16 to 9/9	46	NW50
W3	COMIDA	164.53	72.70	56	ADCP/TCP	W3[d]	N/A	N/A	N/A	NW60
E1	COMIDA	160.50	72.12	40	ADCP/TCP	E1	10–36	8/21 to 9/2	36	NE40
E2	COMIDA	159.12	72.16	51	ADCP/TCP	E2	12–46	8/21 to 8/4	25, 47	NE50
E3	COMIDA	158.55	72.18	56	ADCP/TCP	E3	13–52	8/21 to 6/24	32, 54	NE60
E4	ASL	160.00	71.67	45	ADCP/TC	E4	S/22/40	9/11 to 10/7	43	CPAI02
BC2	BC	159.94	70.92	52	ADCP/TCP	BC2	10–46	9/9 to 8/13	51	BC2
2013–2014 period										
S1	ASL	166.75	71.17	46	ADCP/TC	S1	S/21/35	7/31 to 7/31	44	Crackerjack
S2	ASL	163.28	71.24	45	ADCP/TC	S3	S/17/35	8/1 to 8/5	45	Burger
W1	COMIDA	163.53	72.28	41	ADCP/TCP	W1	10–37	9/10 to 9/20	37	NW40
W2	COMIDA	164.10	72.53	50	ADCP/TCP	W2	12–47	9/9 to 6/16	47	NW50
W3	COMIDA	164.53	72.70	56	ADCP/TCP	W3	N/A	N/A	N/A	NW60
E1	COMIDA	160.50	72.12	40	ADCP/TCP	E1	12–37	9/9 to 9/19	37	NE40
E2	COMIDA	159.12	72.16	51	ADCP/TCP	E2	13–46	9/9 to 9/18	46	NE50
E3	COMIDA	158.55	72.18	56	ADCP/TCP	E3	15–53	9/9 to 9/18	53	NE60
BC2	BC	159.94	70.92	52	ADCP/TCP	BC2	7–46	9/11 to 9/24	46	BC2

[a]ASL moorings recorded velocity at only three depths. S denotes near-surface. [b]Some mooring names are modified based on their locations relative to Hanna Shoal. [c]Data at BC2 and BC5 do not completely encompass this period, but this common period encompasses the shelf moorings, which is the focus of the paper. [d]W3 was not recovered.

present at ~10–15 m depth. Shallower depths are excluded from analysis. Time series with cumulative gaps <10% of the record length were subject to a gap-filling approach (Beckers & Rixen, 2003) that uses the data variance and is statistically more reliable than linear interpolation. We computed low-frequency currents by filtering with a ninth-order 40-hr cutoff low-pass Butterworth filter that effectively removes all variance at periods <30 hr.

For the purpose of presenting shelf-wide circulation patterns, three time periods, focusing on Regions W, S, and E were established. The 2011–2012 period extends from 28 August 2011 to 14 June 2012, the 2012–2013 period runs from 11 September 2012 to 24 June 2013; and the 2013–2014 period ranges from 10 September 2013 to 16 June 2014. Note that BC2, BC5, and BC6 did not record data throughout the entire 2011–2012 period (e.g., BC2 ended on 4 May 2012).

Table 2
Timelines of Strong (≥6 m s^{-1}, ≥2 days) Northeasterly Wind Events

Periods	Year	Period (mm/dd)
2011–12	2011	9/14 to 9/27
		10/3 to 10/6
		10/11 to 10/29
2012–13	2013	1/04 to 1/6
		1/12 to 1/16
		2/21 to 2/26
		3/3 to 3/10
2013–14	2013	9/16 to 9/22
		10/7 to 10/10
		10/19 to 10/23
	2014	1/1 to 1/4
		1/21 to 1/25
		5/30 to 6/2

2.2. Hydrography

The data set includes near-bottom temperature and salinity observations from 17 moorings (Table 1). Temperature/conductivity/pressure (T/C/P) data sampled at 1–15 min resolutions were collected by Seabird SBE 37 MicroCATs and SBE 19 SeaCATs, with temperature and salinity accuracies ~0.01°C and ~0.05, respectively. Middepth T/C/P measurements at E2 and E3 for the 2012–2013 period were also collected. Spurious values and spikes were flagged and removed from the data set manually. Flagged data and episodic gaps (all < ~0.5% of the record length) were filled by linear interpolation.

2.3. Winds and Sea Ice Concentrations

We used the 10-m surface wind field at spatial and temporal resolutions of ~35 km and 3 hr, respectively, from the North American Regional Reanalysis (NARR) model (Mesinger et al., 2006). The NARR grid point (red star in Figure 1a) closest to the E1 mooring is deemed representative of the regional winds. Winds were low-pass filtered with a 40 hr cutoff period. Wind stress (τ_{wind}) estimates follow Large and Pond (1981). We elected to use NARR winds to be consistent with the approach used by Danielson et al. (2014). Moreover, Weingartner et al. (2013) showed that the NARR winds are in excellent agreement with observations.

We used daily satellite-derived passive microwave sea ice concentration (SIC, %) on a 25-km grid (Cavalieri et al., 1996) from 2010–2014 to track sea ice conditions near mooring sites. SIC data were obtained from the National Snow and Ice Data Center (NSIDC, https://nsidc.org/data/nsidc-0051).

2.4. Mean Circulation Patterns

Fang et al. (2017) showed that near-shore (< ~150 km) surface currents during August–October can be substantially changed by strong northeasterly and northwesterly winds. (Northwesterlies were quite rare, so we focus on the impact of northeasterly winds on the circulation.) Strong northeasterly (and northerly) winds can reverse currents in the canyon (Itoh et al., 2013; Weingartner, Potter, et al., 2017) and on the shelf (Stabeno et al., 2018; Woodgate et al., 2005) and induce polynya development in winter (Hirano et al., 2016; Ladd et al., 2016; Weingartner et al., 1998). We define a "weak-wind" flow regime based on all wind events except those for which speeds exceed 6 m s^{-1}. For the strong wind events exceeding 6 m s^{-1} with mean directions from the northeast, the northeasterly flow regime was computed by averaging currents when such wind events have durations of ≥2 days (Table 2), so as to avoid including currents that were still in the process of adjusting to the wind events.

2.5. CEOF Analyses

Complex empirical orthogonal functions (CEOFs) can extract nonstationary narrow-band signals and have been applied to both atmospheric (e.g., Barnett, 1983) and oceanographic (e.g., Auad & Hendershott, 1997; Chavanne et al., 2010) data sets. We employed CEOFs, based on the Hilbert transform, on velocity data to examine propagating, wave-like features at ~3-day period.

The CEOFs were computed as follows. Each velocity component time series at ~25-m depth was filtered with a 50–100 hr passband. This passband was determined from rotary spectra, and ~25 m was selected as it was the depth at which the moorings consistently provided measurements throughout the observed periods. (Note that in 2011–2012 BC6 was not included because the data duration was only 2 months.) We will show that this signal is nearly barotropic, thus the CEOF results are independent of the depth choice. The filtered and Hilbert-transformed velocity data were used to create a covariance matrix for the CEOF computation (Kaihatu et al., 1998). For wave-like, narrow-band series, the resultant eigenvectors are complex with the imaginary component 90° out-of-phase with the real component (e.g., Auad & Hendershott, 1997). For all three observational periods, CEOF Mode 1 explains ~70% of the total variance, whereas Mode 2 explained only ~10% of the variance; hence, only Mode 1 is presented.

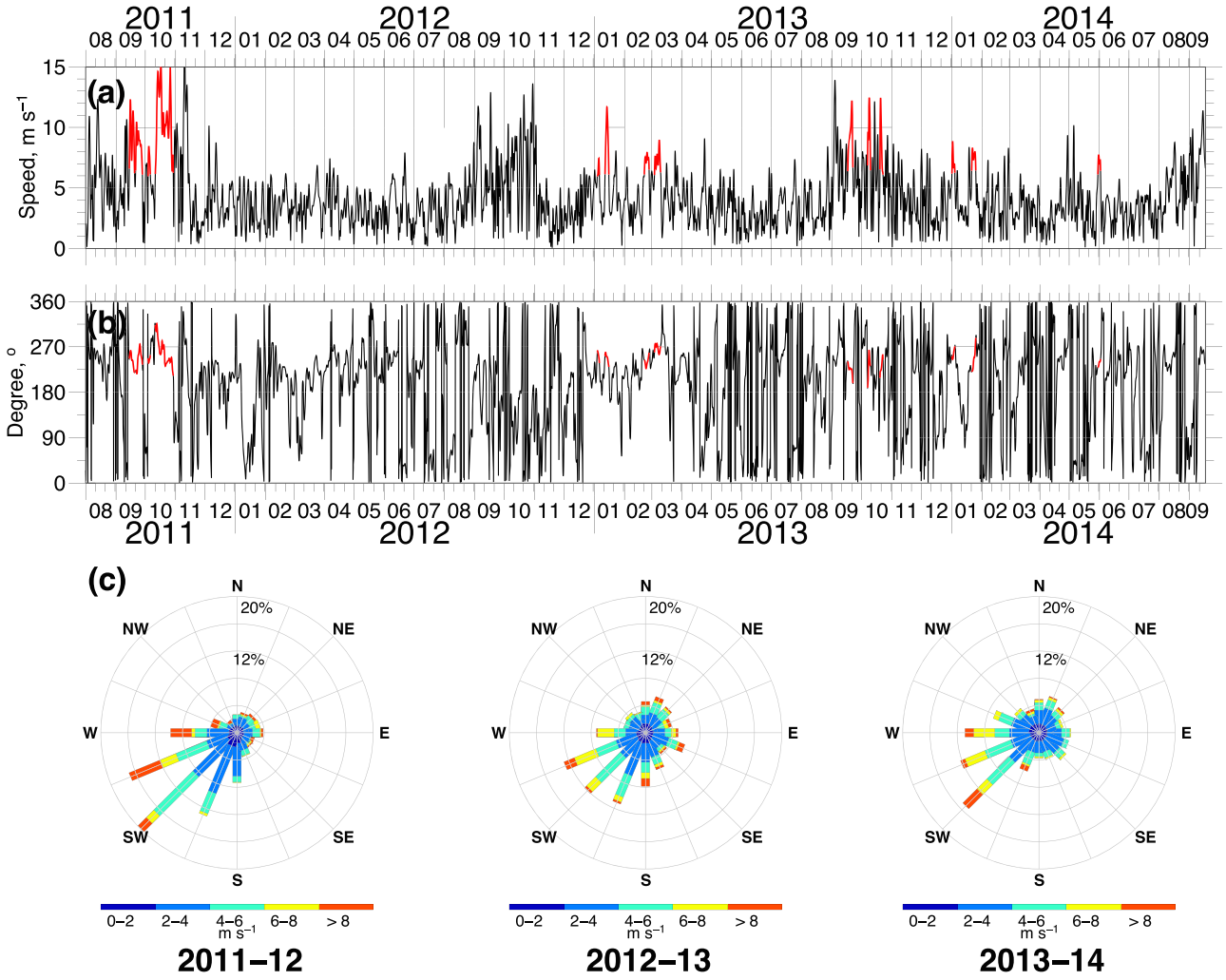

Figure 2. Time series of daily mean wind (a) speeds and (b) directions (in degrees true). Red lines indicate strong wind events from the northeast. (c) Polar histograms of wind velocities in each observational time period. The direction follows oceanographic convention (east = 90°T) and speed is shaded. The percentage indicates frequencies of winds blowing toward that direction.

2.6. EOF Analyses

We examined the spatial structure of the shelf circulation at longer periods (≥8 days) based on an empirical orthogonal function (EOF) decomposition using the vertically averaged currents rotated onto the principal axis after filtering to remove fluctuations at periods <8 days. We then evaluated the representativeness of each EOF based on the correlation between the modal amplitude time series and the vertically averaged velocities for each mooring. We computed the EOFs for each period and separately for the near-surface, near-bottom, and vertically averaged currents. For brevity we show only the vertically averaged results from 2012–2013 as these provide the most spatially comprehensive coverage. Results from the other EOF calculations were similar and not shown.

3. Results

3.1. Winds

During the mooring deployment years, northeasterly winds blew ~40–50% of the time (Figure 2) with the strongest winds (≥10 m s^{-1}) most common in September–October, although episodic wind events with speeds ≥5 m s^{-1} also occurred in winter. Winds over the three periods were, on average, northeasterly (~237°T) at ~1.6 m s^{-1}. There were no substantial differences among the periods, with two exceptions. In

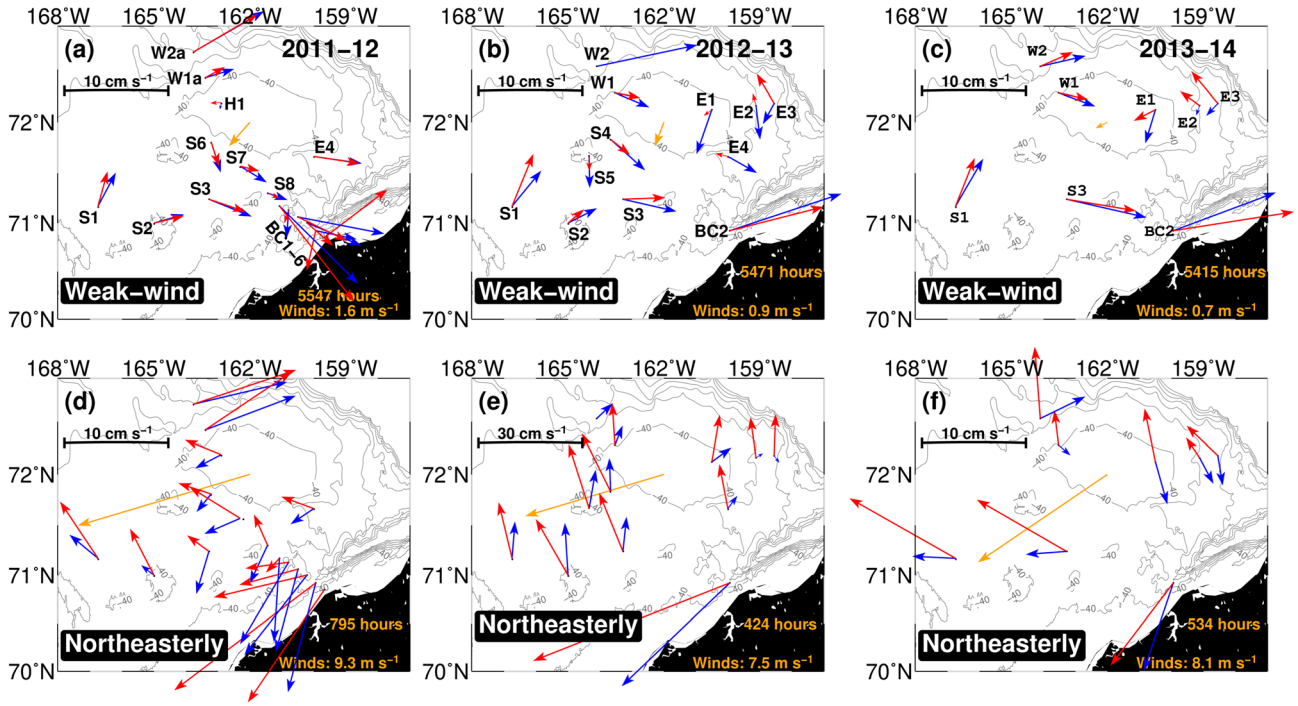

Figure 3. Weak-wind circulation patterns for the (a) 2011–2012, (b) 2012–2013, and (c) 2013–2014 periods, respectively. Velocity vectors near the surface and bottom are shown in red and blue, respectively. The orange vectors signify the mean wind vector with its magnitude and accumulated hours given in the lower right corner of each map. Various mooring names are provided. Panels (d), (e), and (f) are the same as (a), (b), and (c) but for northeasterly flow regimes. Note that the vector scale is different in (e).

fall 2011, wind speeds were greater than in the other years and from late December 2012 to early April 2013, winds were generally northeasterly at speeds <5 m s^{-1}, but with occasional greater speeds. We show later that these exceptions substantially affected the shelf's hydrography.

3.2. Circulation

3.2.1. Weak-Wind Circulation Pattern

The mean weak-wind circulation patterns for each of the three time periods are shown in Figures 3a–3c and include the corresponding mean wind vector. On average these winds had speeds of < ~2 m s^{-1} and were from the northeast ~50% of the time, but with directional variability. Within Region S, the flow was north-northeastward in the Central Channel (mooring S1) at ~5 cm s^{-1}. Closer to the Shoal (moorings S6–S8 in 2011–2012 and moorings S4–S5 in 2012–2013) the flow was southeastward at ~3 cm s^{-1}. Based on limited summertime hydrography, Weingartner, Dobbins, et al. (2013) speculated on such a flow while Pickart et al. (2016) detected it from two comprehensive summer shipboard surveys. The moored data corroborates both findings and indicate that this flow is a year-round circulation feature along the southern flank of the Shoal that draws waters from the Central Channel and/or the west side of the Shoal. Currents at the other moorings in Region S were nominally eastward at ~5 cm s^{-1}. The small shears and turning angles of < ~20° between the near-surface and near-bottom velocity vectors attest to the largely barotropic character of the flow in Region S. As the currents south of Hanna Shoal (e.g., moorings S3–S8 and offshore BC moorings) approach the head of Barrow Canyon (they veer northeastward and accelerate ~10 cm s^{-1}). These findings are consistent with previous observations (Stabeno et al., 2018; Weingartner et al., 2005) and models (Spall, 2007; Winsor & Chapman, 2004). The weak currents (<1 cm s^{-1}) atop Hanna Shoal (e.g., H1) reflect flow stagnation either by local topographic obstruction or via Taylor column dynamics as suggested by Martin and Drucker (1997).

Along the west side of Hanna Shoal and in water depths >40 m (Region W; moorings W1a, W2a in 2011–2012 and mooring W2 in both 2012–2013 and 2013–2014) the flow is northeastward and comparatively swift (~10 cm s^{-1}). Again the vectors suggest a barotropic flow turning anticyclonically toward the north side

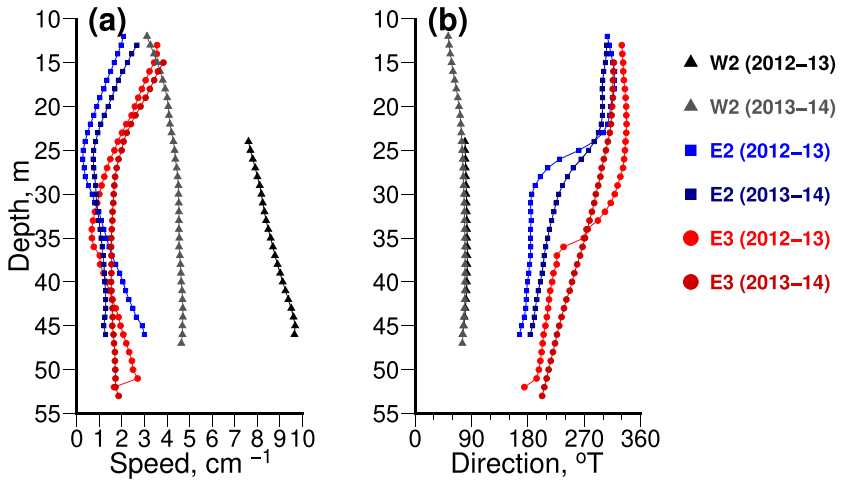

Figure 4. (a) Vertical profiles of averaged current speeds at moorings W2 (triangle), E2 (square), and E3 (circles) in the 2012–2013 and 2013–2014 periods. (b) Same as (a) but for averaged directions (in degrees true).

of the Shoal. At W1 (40 m water depth) the current was ~3 cm s^{-1} southeastward toward the center of the Shoal, although it is unclear, if this is a result of the flow steered by the local bathymetry or if it actually feeds Region S.

In contrast to Regions S and W, the flow in Region E, especially in water depths >40 m (moorings E2–E4 in 2012–2013, Figure 3b), exhibits considerable vertical shear. At E2 and E3 the near-surface currents were northwestward but bottom currents were stronger and southward. At E4, the deep flow was eastward toward Barrow Canyon, while the surface flow was westward albeit considerably weak. In summary, the deep currents in Regions W and E are approximately aligned along isobaths and suggest anticyclonic flow around Hanna Shoal. However, whereas the surface currents west of the Shoal comply with this depiction, those at E2 and E3 do not. Our results indicate that here the upper-layer (< ~35 m) flow is decoupled from the barotropic forcing that presumably dominates the deep flow (Figure 4). This is revealed by the veering of the currents changing most significantly near ~25–35 m at E2 and E3, along with an increase in current speeds above these depths. As shown by Weingartner, Fang, et al. (2017) the shelf east of Hanna Shoal is strongly stratified in summer and the upper-layer currents are baroclinic (cf. their Figure 14), controlled by horizontal salinity gradients, and flow northwestward at velocities of ~10 cm s^{-1}. The mooring data indicate that the current shear in Region E persists year-round.

The southward flow at depth at E2, the persistent northeastward flow at W2, and the mean eastward flow along the 30-m isobath north of Hanna Shoal (Stabeno et al., 2018) supports the notion of an anticyclonic circulation around Hanna Shoal (Spall, 2007; Winsor & Chapman, 2004). Based on the findings of Weingartner, Potter, et al. (2017) and those reported here, it appears that the deep flow is deflected toward Barrow Canyon but not carried onto the shelf south of Hanna Shoal. Although the deep currents are in agreement with this circulation scheme, the mean transport around the Shoal is not. Indeed, the mean vertically integrated transport between E2 and E3 (on the 50 and 56 m isobaths) is not statistically significant from zero over the 2 years of measurements. The mean transports can be separated into upper-layer (< ~25 m) and lower-layer (> ~25 m) components. The upper- and lower-layer transports are of opposite sign and have mean (and statistically significant at $p < 0.05$) magnitudes of ~0.01 Sv for the two observational periods, suggesting that the upper ocean flow is comparable to the deep transport. We next estimated the transport along the west side of Hanna Shoal by assuming that the flow at W2 is representative of the flow over the same pair of isobaths (i.e., 50 and 56 m isobaths). Here the mean transports were northeastward at ~0.1 and ~0.05 Sv in 2012–2013 and 2013–2014, respectively, and statistically ($p < 0.05$) different from zero. The results imply along-isobath flow convergence north of Hanna Shoal, which must be compensated for by a cross-isobath flow.

The weak-wind circulation regime is dramatically altered under strong (≥6 m s^{-1}) northeasterly winds (Figures 3d–3f). Under such winds the flow is reversed in Barrow Canyon. In Region S, near-surface

currents were typically 10–20 cm s^{-1} to the right of the wind whereas the deeper flows varied among the periods. In 2011–2012 and 2013–2014, when most of the northeasterly wind events occurred in the fall (Figure 2, Table 2), the deep currents were westward or southward. In 2012–2013, these flows were northward when all of the northeasterly wind events occurred in winter and ice covered the shelf. While the differences may be due to the averaging periods used in forming the composites, other factors may have been at play. These include an anomalously large inflow from Bering Strait in January and March 2013 (Woodgate, 2018), which may have contributed to a larger northward flow over the shelf. There were also several large coastal polynya events during that winter, which would have resulted in dense water spreading seaward of the polynyas.

Although northward flow in the Central Channel effectively ceased during the northeasterly winds in 2011–2012 (Figure 3d) and 2013–2014 (Figure 3f), the deep eastward flows west of Hanna Shoal did not weaken but intensified. The situation on the east side of Hanna Shoal is less clear, except in 2013–2014, when the deep flow east of Hanna Shoal increased under northeasterlies. In their modeling study, Pickart et al. (2011) showed that eastward flow extended across the entire outer Chukchi shelf under similarly strong winds and strengthened the anticyclonic circulation around Hanna Shoal.

3.2.2. Flow Variability

Before exploring the temporal and spatial structure of the circulation and hydrography of the shelf, we briefly outline some aspects of the variability over the shelf by showing selected time series of the mean daily vectors of the bottom currents and the winds from 2012–2013 (Figure 5; which also lists the principal axis orientation and the fraction of current variance accounted for by this axis). First note that over much of the region, but especially in Barrow Canyon, Region E, W2, and S1, the variability is primarily rectilinear insofar as ~75% or more of the variance is aligned along the principal axis. However, ~2/3 of the variance is constrained to the principal axis even for the more gently sloping portions of Region S (e.g., S3; also S2, S4, and S5, not shown). Second, the variability was largest in fall and least in spring and summer, when the winds were generally weaker. Third, reversals are more common and more energetic in Barrow Canyon (note the scale difference compared to other sites) than elsewhere. Here reversals of several days duration occurred in fall and there was a prolonged reversal (coincident with episodic polynya formation along the coast) from mid-December through February. From March to the end of the record, however, the currents were northeastward and steady. At the other extreme, bottom currents were remarkably steady at W2, and in Region E (e.g., E2; also E1, E2, and E4, not shown) throughout the year. The currents at W1 fluctuated in all directions. For W2, the only reversal occurred in late September 2012, whereas in Region E, the largest disruption occurred from late February to mid-March, when the currents were northward. The persistent eastward flow at W2 appears to have little relationship with the regional winds in agreement with Stabeno et al. (2018) for currents along the northern rim of Hanna Shoal. Nor do the flow variations at W2 appear to correspond much with those at S1 (within the Central Channel). However, across much of Region S the current fluctuations appear coherent with one another and with the winds. In the following three sections we explore aspects of the current variability as a function of frequency.

3.2.3. Flow Variability: Frequency Domain Perspective

Rotary spectra (e.g., Emery & Thomson, 1997) of the unfiltered currents at 25 m for 2012–2013 and 2013–2014 at W2 and E2 (Figures 6a–6d, respectively) differ prominently from one another in two ways. First, for frequencies between the local inertial (~0.0796 cph) and the semidiurnal tide (0.0805 cph for the M_2 tide), the spectra at E2 (and at E1 and E3) are considerably broader than those at W2 (with similarly narrow spectral widths occurring elsewhere on the shelf). The broadening of the spectral widths at these tidal frequencies is possibly associated with internal tides as Kulikov et al. (2004) documented for the heavily stratified Mackenzie shelf. The second noteworthy difference between the spectra is that the clockwise (CW) energy is significantly greater than the counterclockwise (CCW) energy at periods of 50–100 hr at E2 (gray-shaded region in Figures 6b and 6d), whereas there is no significant difference between the CW and the CCW energy in this band at W2 (gray-shaded region in Figures 6a and 6c). The predominance of CW energy over CCW energy at these periods was observed at most other locations, although not in Barrow Canyon or in the Central Channel at S1. The spectra (Figures 6b and 6d) indicate that at E2 CW energy is somewhat greater than CCW energy at higher frequencies (i.e., up to the K_1 frequency). However, these differences are not apparent elsewhere on the shelf, except at E3. Thus, our subsequent focus is on the signal at periods of 50–100 hr.

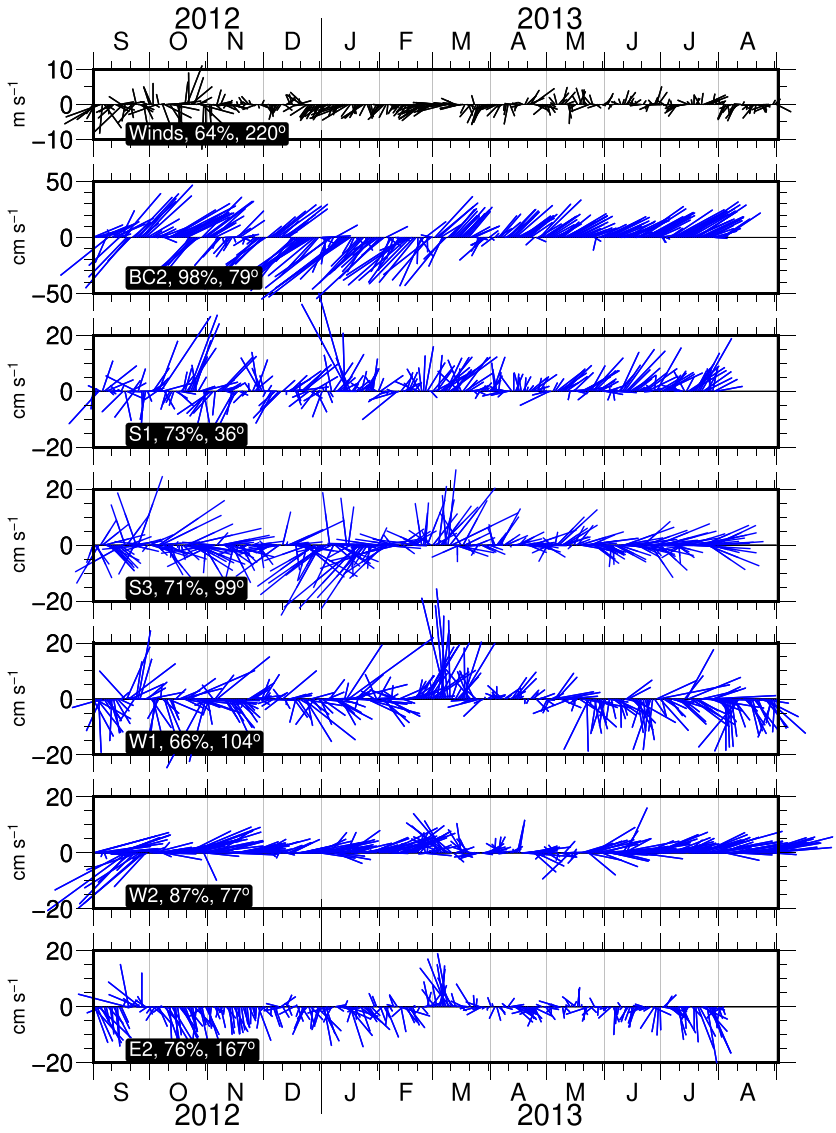

Figure 5. Wind (black) and bottom current vectors (blue) for the 2012–2013 period. North is oriented toward the top of the page. Principal axis orientation (in degrees true) and percent variance (%) explained by this axis are listed adjacent to the mooring name.

We next examined the scalar and rotary coherences in the 50–100 hr band between moorings sites and vertically at each location. The coherence spectra (not shown) are significant at the 95% confidence level at these periods and the vertical phase spectra imply a barotropic signal. The coherence spectra between E2 (or E3) and E4 in Region E yield a phase difference of 70–120°, implying that the signal propagates southward from the northeast side of the Shoal. If we assume a central period of ~75 hr and a phase difference of ~100°, then the signal takes ~20 hr to propagate the ~60-km distance from E2 (or E3) to E4 and implies an along-isobath phase speed of ~0.8 m s^{-1}. In aggregate the results suggest a clockwise-propagating barotropic topographic wave that starts along the northeastern side of Hanna Shoal and eventually propagates westward around the south side of the Shoal.

3.2.4. Topographic Wave Mode

To examine this hypothesis of barotropic topographic wave in more detail we show a ~1-month time series in January 2014 of the mean daily τ_{wind} (Figure 7a) and the 50–100 hr band-passed currents at E1 (Figures 7b and 7c), which highlights the episodic nature of the waves. Each episode appears as striped patterns of positive-negative velocities throughout the vertical throughout the time series. The time series clearly

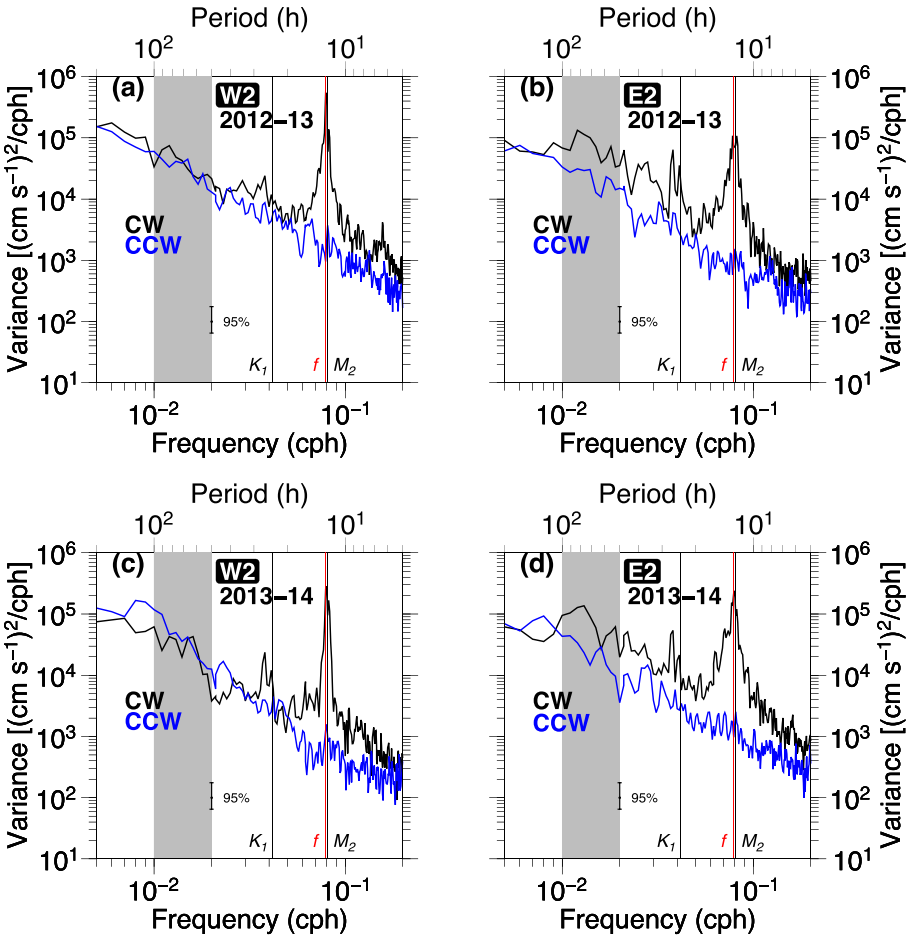

Figure 6. Rotary spectra computed from unfiltered 2012–2013 data at (a) W2 and (b) E2. Panels (c) and (d) are the same as (a) and (b) but for 2013–2014. Clockwise (CW) and counterclockwise (CCW) components are in black and blue, respectively. Vertical black lines indicate the K_1 and M_2 frequencies, and the vertical red line indicates the inertial frequency at 72°N. The gray-shaded area denotes the frequency band that is equivalent to the period of 50–100 hr.

shows three pairs of positive-negative oscillations from 19–28 January, which are consistent with a ~3-day period. From examining the ~2-year long time series, the wave packets do not seem to have any preferred seasonality (not shown), although they mostly coincide with wind stress pulses (Figure 7). Not all of the signals appear to be in-phase with these pulses, however, suggesting that they might have originated elsewhere.

The CEOF analyses provide a broader perspective on the propagation characteristics of the waves (Figure 8). The figures show the Mode 1 complex eigenvectors for the three different periods and include the potential vorticity contours (i.e., f/h, where f is the local Coriolis parameter and h is the local depth) along which topographic waves propagate. Eigenvectors with a phase difference of ~90° between their real and imaginary parts are consistent with coastal trapped waves (Auad & Hendershott, 1997). As evident in Figures 8a–8c, the real parts of the eigenvectors are very small and thus poorly resolved and/or out-of-phase with the imaginary component west of Hanna Shoal (W1a, W2a, W1, and W2) and in the Central Channel (S1). Similarly, the imaginary component of the eigenvectors at BC2 has considerably smaller amplitude than their real counterparts (e.g., Figure 8b and 8c). The eigenvectors show an out-of-phase tendency near Barrow Canyon and the Central Channel (e.g., Figure 8a, BC1–BC3; Figures 8b and 8c, S1). These features suggest that the waves do not reach the Central Channel or enter Barrow Canyon, where the large cross-shore gradient in f/h presumably blocks onshore wave propagation (Miller et al., 1996). These findings are consistent with the absence of a significant CW spectral peak in the Central Channel, Barrow Canyon, and northwest of Hanna Shoal. In aggregate, these results indicate that the wave signals predominate east and south of Hanna Shoal (e.g., Figure 8a, S6–S8; Figure 8b, E2–E3, S4–S5; Figure 8c, E1–E3).

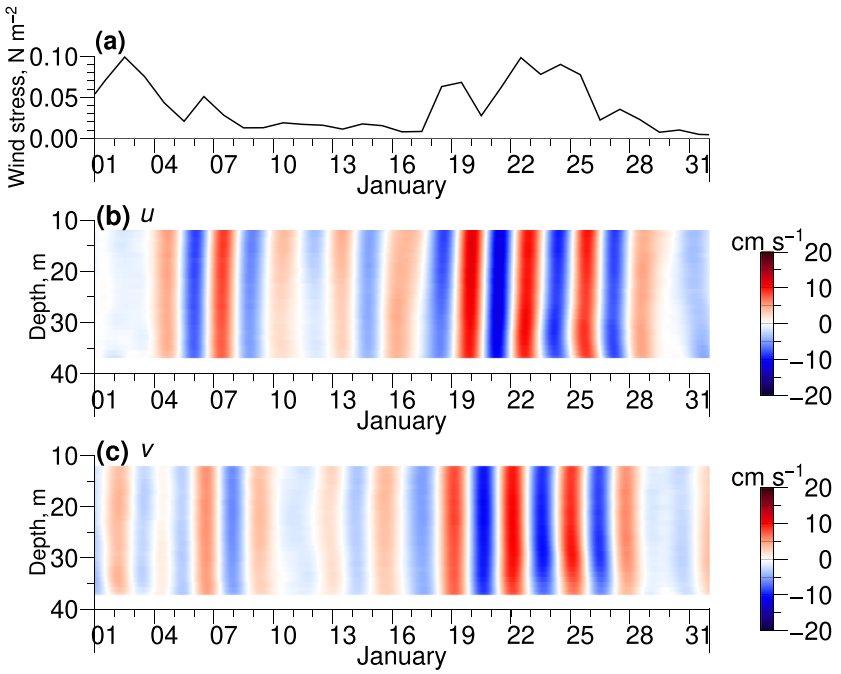

Figure 7. Time series at E1 in January 2014 of (a) wind stress, (b) profiles of the zonal velocity component filtered by a 50–100 hr passband, and (c) same as (b) but for the meridional component.

The CEOFs enable the investigation of how phase changes with time by applying a least squares fit to the unwrapped phase time series for Mode 1. Doing so yields wave periods of ~3.2 days (~77 hr), ~3.1 days (~74 hr), and ~3.5 days (~84 hr) for the 2011–2012, 2012–2013, and 2013–2014 periods, respectively. When applied to the dispersion relation for barotropic topographic waves propagating over a uniformly sloping bottom (e.g., Cushman-Roisin & Beckers, 2011), these periods yield along-isobath wavelengths of ~180–200 km and phase speeds of ~0.6–0.8 m s^{-1}. The latter values corroborate the coherence results mentioned previously.

3.2.5. Longer-Period (≥8 days) Flow Variability

The EOF results based on the vertically averaged currents from 2012–2013 are presented in Figure 9 and Table 3. Mode 1 captures 45% of the variance and its spatial domain consists primarily of the Hanna Shoal E1–E3 moorings (including moorings S4 and S5 south of the Shoal). Mode 2 accounts for 29% of the

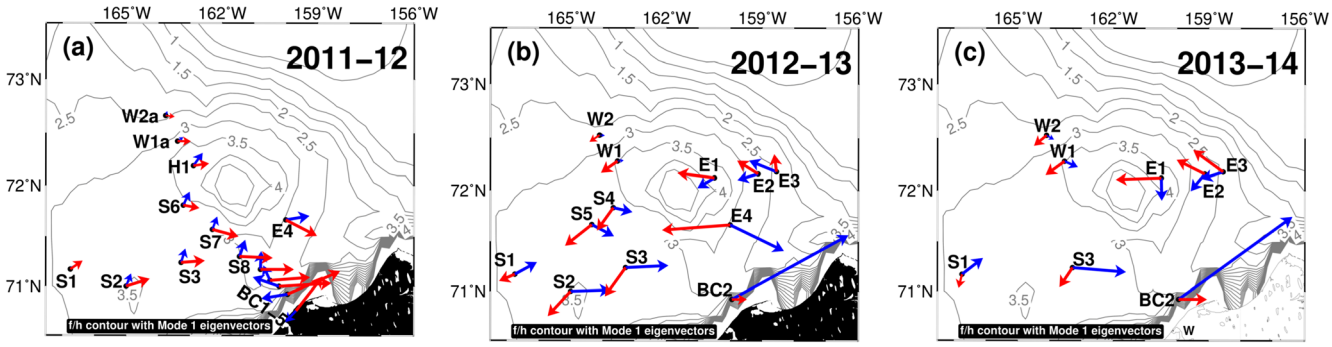

Figure 8. CEOF eigenvectors of Mode 1 of the (a) 2011–2012, (b) 2012–2013, and (c) 2013–2014 periods. Note that measurements in a fall within 30 August 2011 to 3 May 2012. Currents at time t_0 are blue (real component of eigenvectors), whereas currents at $t_0 + \pi/2$ are red (imaginary component of eigenvectors). Names of mooring sites are provided in each panel and f/h (10^{-6} m^{-1} s^{-1}) contours are in gray.

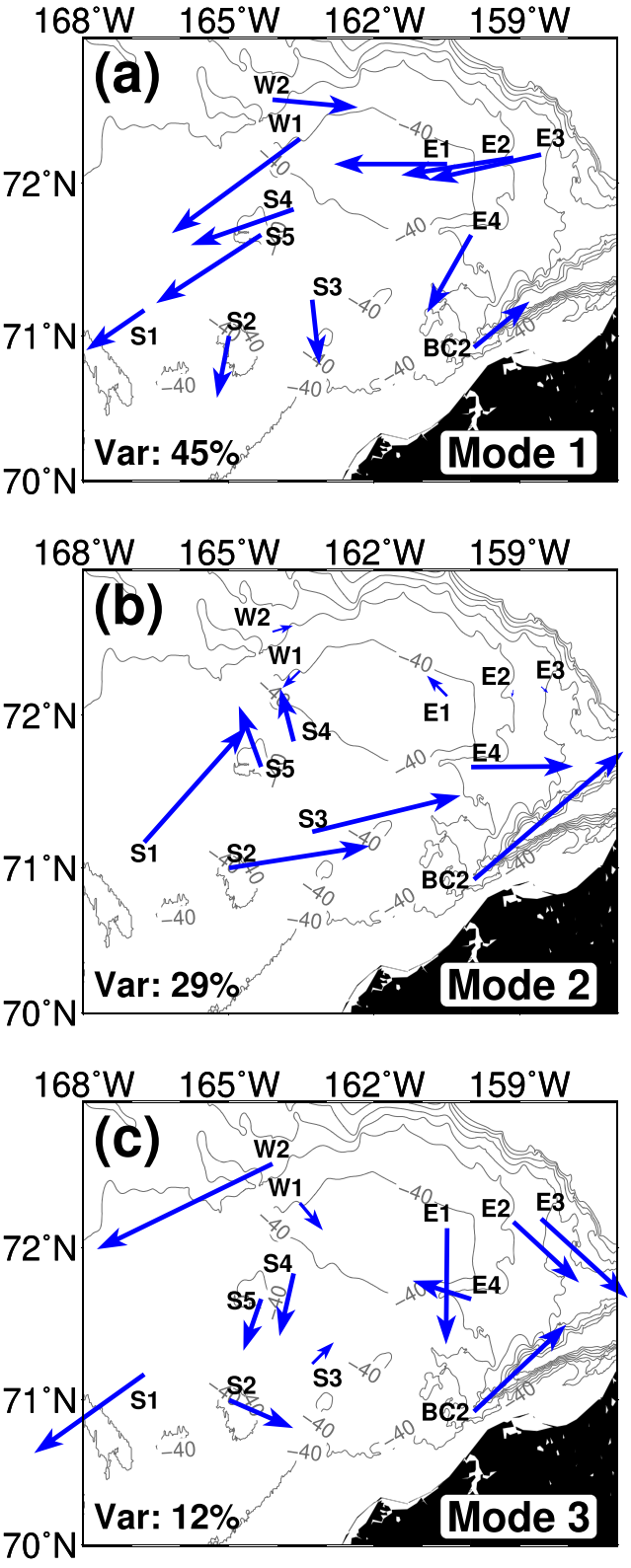

Figure 9. EOF eigenvectors and percentage of variance explained by (a) Mode 1, (b) Mode 2, and (c) Mode 3, respectively. EOFs are based on vertically integrated velocities from 2012–2013.

variance and it encompasses Region S (except S4 and S5), Region C (Barrow Canyon), and mooring E4 on the east side of the Shoal. Although Mode 3 only accounts for 12% of the variance, the correlation coefficients imply that this mode is capturing variations primarily along the west side of Hanna Shoal (W2) and to some extent the Central Channel (S1). We assessed the relationship between the winds and the three modes through a multiple linear regression of the modal amplitude time series against the winds over the Chukchi Sea, Bering Strait, and the Bering Sea shelf following Danielson et al. (2014). Physically, the relationship incorporates the response of Chukchi shelf currents to northward propagating shelf waves. For Mode 1, the regression explains 29% of the variance, with the Chukchi and Bering Strait winds dominating the regression. The regression accounts for 47% of the variance in Mode 2 with all three sites contributing. For Mode 3, the regression is not statistically significant as it explains only 8% of the variance.

In a retrospective study, Lin et al. (2019) objectively mapped the summer circulation over the northeast Chukchi shelf using vertically averaged shipboard ADCP data. They compared their maps to the wind stress curl and found events in which the flow north of Hanna Shoal was convergent (westward flow east of Hanna Shoal and northeastward flow west of the Shoal) when the curl was positive. They also found negative curl events in which the circulation around the Shoal was anticyclonic and concluded that the circulation is sensitive to wind stress curl. We found no correlation between our EOF modes and the curl, suggesting that while the curl may be responsible for some of the circulation variability in summer, it does not do so in a statistically significant manner throughout the year, with respect to the low-frequency motions considered here.

3.3. Hydrographic Variability

Time series of near-bottom temperature and salinity from the moorings are presented in Figures 10 and 11, respectively. Each series is overlain with the SIC time series derived from the pixel closest to the mooring. (The thermohaline data from the Barrow Canyon mooring were presented by Weingartner, Potter, et al., 2017 and are not shown here.) Distinct annual cycles in temperature are apparent at each mooring site. Below, we will first consider Region S. Beginning in late May or June near-bottom temperatures slowly begin increasing from the freezing point with this warming accelerating by late July. Maximum temperatures occurred as early as August or September at the more southern moorings (e.g., S1–S3) well before ice appeared. Thereafter, cooling began, although the rate of cooling varied among years. For example, cooling proceeded very rapidly at S1 in the fall of both 2011 and 2013, and occurred some 2–4 weeks before ice appeared in middle to late November. In both of these years and at these three sites temperatures decreased to the freezing point by early December. By contrast, in the fall of 2012 the temperature maxima were 1–2°C lower than in 2011 and 2013, cooling progressed more slowly, and the freezing point was reached at a later stage (mid-January). Maximal temperatures appear to occur somewhat later at the more northern moorings in Region S. For example, S4 and S5 attained their maxima some 1–2 months later than S2 and S3 (not shown), and about 2 weeks after ice was present. The annual temperature cycle was similar in Region W although here the temperature maxima lagged those of Region S. Hence, the maxima occurred in early January 2013 at W1 and

Table 3
Correlation Coefficients Between EOF Modes and Velocity Records From Each Mooring

Mooring	Mode 1	Mode 2	Mode 3
E1	**0.82**	0.02	<0.01
E2	**0.81**	<0.01	0.07
E3	**0.77**	<0.01	**0.12**
E4	0.14	**0.47**	0.06
S2	<0.01	**0.82**	0.07
S4	**0.92**	0.01	<0.01
S5	**0.86**	0.03	<0.01
S3	<0.01	**0.95**	<0.01
S1	**0.22**	**0.46**	**0.21**
W2	**0.40**	0.02	**0.46**
W1	**0.92**	0.01	<0.01
BC2	0.15	**0.69**	**0.11**

Note. Values in bold indicate statistically significant at the 95% level.

W2, some 2 months after it appeared at S1 and 2 weeks after the maximum at S4 (not shown). At most of the moorings, the temperatures varied quite rapidly over the course of about 2 weeks prior to collapsing to the freezing point. Similarly rapid salinity fluctuations occurred (Figure 11), which preceded bottom freshening and the annual salinity minimum. Most likely, these rapid fluctuations are signatures of the erosion and sinking of the pycnocline through convection and mixing. Hence, in Regions S and W, we assume that once near-bottom temperatures decrease to the freezing point and salinities collapse to their minimum values in late fall or early winter, the water column becomes unstratified and remains so until summer melt commences. In these regions the near-bottom temperatures generally remained at the freezing point until the following June when the annual cycle began anew.

An in-depth analysis of the causes for the interannual differences in the fall cooling rate is beyond the scope of this paper, but as an aside we note at least three contributing factors. First, the water column in summer and fall of 2011 was more weakly stratified than in 2012 and 2013 (Weingartner, Fang, et al., 2017). In part this was due to the nearly complete absence of ice from the shelf (including Hanna Shoal) by late July of that year, whereas in the other 2 years, ice remained over Hanna Shoal through early September. Second, SIC maps show considerable differences in fall ice extent among the three years. By mid-November 2011, much of the Chukchi shelf, with the exception of the northern half of Barrow Canyon, was still ice-free with the 75% SIC contour lying north of 73°N. In contrast this isopleth was between 70.5° and 71°N on the same date in 2012 but somewhat farther north (~72°N) by mid-November 2013. Although the year 2012 reached a record low Arctic sea ice cover on 13 September (Parkinson & Comiso, 2013), sea ice cover advanced from ~73.5°N to ~71°N in 2 weeks after 31 October. Hence, the high SIC in 2012 provided a greater degree of insulation over the northeast Chukchi shelf compared to the other years. Finally, the September through November integral of the wind speed cube (proportional to the rate at which wind mixes the water column) was twice as great in 2011 than in the other years. Collectively, these differences are consistent with the notable delay in fall cooling observed in 2012.

The annual temperature cycle for near-bottom waters east of Hanna Shoal (Figure 10; moorings E1–E4) shares some similarities with the other regions, although it is remarkably different in the time at which these waters reached freezing and the persistent stratification. Here maximum temperatures occurred in January in the winter of 2012–2013 (and in December 2013 at the beginning of the following winter at mooring E1–E3) similar to Region W. However, at moorings E2 and E3, the near-bottom temperatures remained 0.2–0.8°C above freezing throughout most of winter and spring. (At E2 there was a brief drop in temperature to the freezing point in March due to a northward surge of recently formed salty winter water. This surge was also detected at E1 and E4, but not at E3.) In contrast middepth temperatures were at freezing point. Near-bottom temperatures reached the freezing point only in June or August well after sea ice began melting in May, implying that these cold waters are due to advection and not local freezing. Moreover, the water column remained heavily salt-stratified throughout winter (Figure 11) at E2 and E3. For example, the vertical salinity gradient at E2 was ~0.1–0.23 m^{-1} in December and January. (In fact, the winter vertical salinity difference over the water column at this time is comparable to that observed in the summer; Weingartner, Fang, et al., 2017). Although the gradient weakened thereafter, it was still substantial at ~0.05 m^{-1}.

Freezing temperatures appeared in March 2013 at E1 and E4 and were associated with the northward surge of WW along the east side of Hanna Shoal at that time (e.g., Figure 5). These signals appeared ~3 months earlier than at E2 and E3 but ~1.5 months later than in Regions S and W. Temperatures remained at freezing point at E1 thereafter, whereas temperatures at E4 fluctuated between freezing and slightly above (by ~0.5°C) freezing point until late July. Mooring E4, situated at ~71.7°N, is slightly north of the zonally oriented front found in summer and fall along 71.5°N (Fang et al., 2017; Lu et al., 2015; Weingartner, Fang, et al., 2017). This front separates less-stratified BSW south of the front from the heavily stratified water column (consisting of dilute meltwater atop dense winter waters) to the north. However, this front (and the heavy stratified region north of it) was absent in 2011, when little meltwater was present over and east of

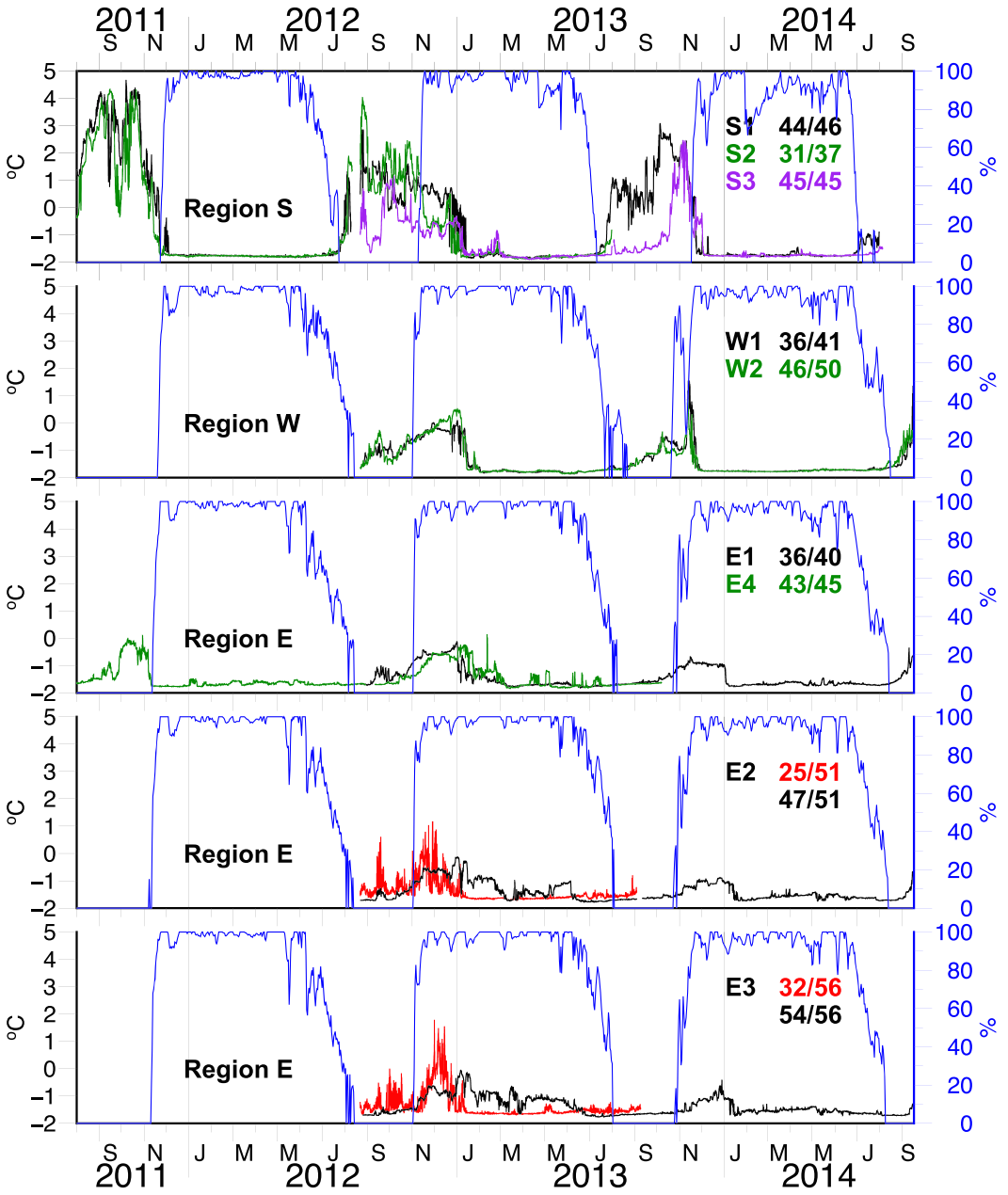

Figure 10. Time series of near-bottom potential temperatures at the selected moorings shown in different colors (black, green, and purple), and SIC (blue) nearest to S1, W1, E1, E2, and E3. The ratios nn/mm denote the sensor and water depths (m), respectively. The red lines for moorings E2 and E3 denote middepth potential temperatures.

Hanna Shoal. In 2011, temperatures at E4 reached the freezing point in November, similar to the other sites in Region S, and likely a consequence of the absence of stratification.

The other noteworthy feature in these time series is the abrupt salinity increase that began in late February and continued through mid-March across much of Region S, in particular at S1, S2, S3, but also at E4 (Figure 11, see black arrows). This freezing, highly saline (dense) water formed along the west coast of Alaska in a large polynya, which developed intermittently between January and through mid-March (see also Stabeno et al., 2018). The dense waters would have spread westward in two ways. One is via the eddy mechanism of Gawarkiewicz and Chapman (1995). The other is by advection by the background circulation. Initially, the dense water flowed southwestward in the coastal flow as observed in Barrow Canyon (Figure 5;

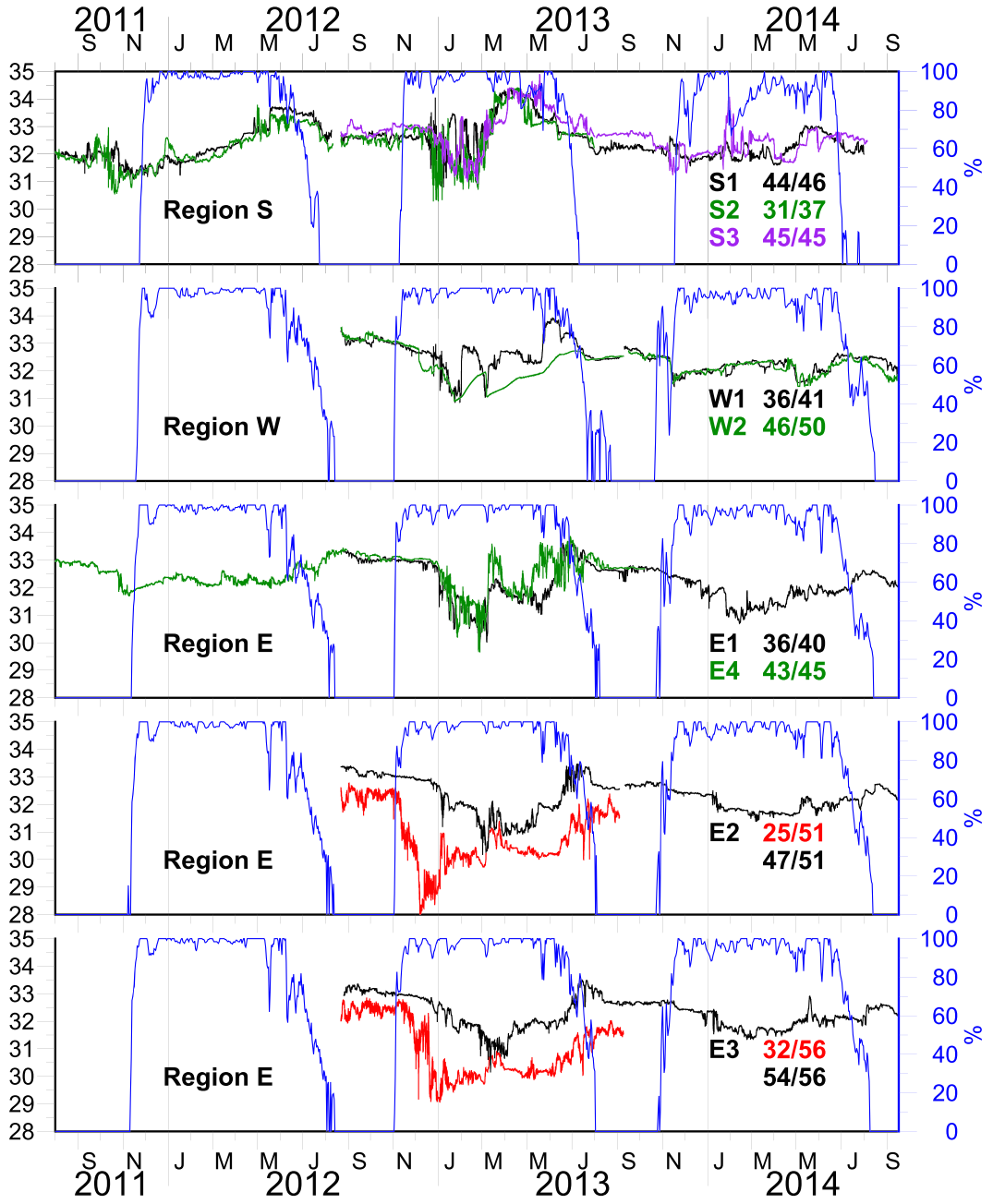

Figure 11. As in Figure 10, but for salinity. Black and red arrows indicate high-salinity events (see text).

Weingartner, Potter, et al., 2017). This flow subsequently reversed and carried the dense water northward throughout Region S and along the coast such that salinities increased rapidly from late February through mid-March. The increase occurred in a series of steps at S1, S2, and S3 with maximal salinities of ~34.4 observed in April at all sites. The same signal, with diminished salinities (~34.1) arrived at S4 and S5 in early May (not shown) and at W1 in the latter half of May. Salinity also increased briefly by ~1–2 in mid-March at E4 and E2 (but not at E3) before decreasing again. We ascribe these salinity fluctuations to the brief period of northward advection of dense water from Region S, although this flow event was of insufficient duration to transport the saline water to E3. Afterward, the bottom flow reverted to its weak-wind condition (Figures 3a, 3c, and 3e) and advected fresher water into Region E. Maximum salinity (~33.5**)** water only arrived at E1 and E2 in June and at E3 in July (Figure 11, see red arrows). This

saline water is most likely the diluted remnant of the high-salinity water observed in March at W1. Its arrival at E1 and E2 in late June followed the sustained period of southward bottom flow that resumed in mid-March at these sites (Figure 5). This observation suggests that the dense water was carried eastward around the north side of Hanna Shoal and then southward along the eastern side of the Shoal. And, in good agreement with the findings of Stabeno et al. (2018), it also implies a mean speed of ~5 cm s^{-1} around the northern flank of Hanna Shoal.

Surprisingly, no such high-salinity signals appeared at W2. Although there was a salinity increase in March it did not exceed 32 and maximum salinities of ~32.7 occurred in June; that is, the values were considerably lower than those simultaneously observed at both W1 and in Region E. Apparently, the high-salinity water was trapped to depths <50 m in Region W and only began to descend to greater depths after rounding the western side of the Shoal.

4. Discussion and Summary

Our observations indicate that the circulation and hydrography east of Hanna Shoal are quite different from the shelf regions south and west of the Shoal in two major ways. First, the former region includes persistent year-round stratification with dilute, surface meltwaters capping saline, near-freezing bottom waters. By comparison, the regions south and west of Hanna Shoal are less stratified in summer (and likely well-mixed in winter). The stratification northeast of the Shoal is maintained by a variety of processes, including the persistence of melting ice in summer, occasional onshore advection of low-salinity surface waters from the slope and Barrow Canyon (Weingartner, Fang, et al., 2017), and westward advection of dilute Beaufort shelf waters (Weingartner et al., 2017). In a recent study Li et al. (2019) finds that the shelf-break jet reverses under strong northwesterly or northeasterly winds, resulting in onshore flow toward the shelf east of Hanna Shoal (cf. their Figure 17). We suspect that shelfbreak/slope waters would be advected subsequently to Region E, thus maintaining the stratification east of the Shoal. The stratification differences likely contribute to the broader spectral widths at the semidiurnal frequency, in Region E compared to Region W.

Second, the velocity field is vertically sheared with westward or northwestward flow in the upper layer and southward flow along the bottom. While some of this shear may be an onshelf extension of the Chukchi Slope Current (Corlett & Pickart, 2017; Li et al., 2019), it is also a consequence of the northeasterly winds and, at least in summer, a cross-shelf density gradient (Weingartner, Fang, et al., 2017). By comparison, the regions south and west of Hanna Shoal are less stratified in summer, probably well-mixed in winter, and only weakly sheared by the wind.

The dynamic coupling among Hanna Shoal, Barrow Canyon and Region S (south of the Shoal) varies as a function of the forcing frequency. At periods of about 3 days topographic waves are generated episodically and propagate anticyclonically onto the southern shelf. Although the large f/h gradient blocks the waves from propagating into Barrow Canyon they were also not detected west of Hanna Shoal. The reason for this is uncertain, although the wave scattering arguments of Yankovsky and Chapman (1995) may apply. They showed that in the presence of mean current shear the number of freely propagating wave modes is reduced and that convergence of f/h contours induces shorter scale oscillations and scattering into higher, more slowly, propagating modes, which can quickly decay. Along the west side of Hanna Shoal the currents are horizontally sheared (e.g., Figure 3a) and the f/h contours converge so both effects may contribute to wave scattering.

At periods ≥8 days the EOF results indicate weak coupling between the circulation around Hanna Shoal and that over the shelf south of the Shoal and in Barrow Canyon. In the latter two regions the dynamics are consistent with a barotropic response to regional and remote (Bering Strait and the Bering Sea shelf) winds, which account for nearly half of the current variance here. In contrast these winds explain <1/3 of the current variance around Hanna Shoal. Moreover, current fluctuations at W2 (at 50-m depth northwest of Hanna Shoal) appear to be only weakly associated with those in the Central Channel and unrelated to the wind.

This finding and the persistent northeastward flow at W2 along the west side of Hanna Shoal suggests that here the flow is connected to the western Chukchi Sea with waters flowing eastward from Herald Canyon

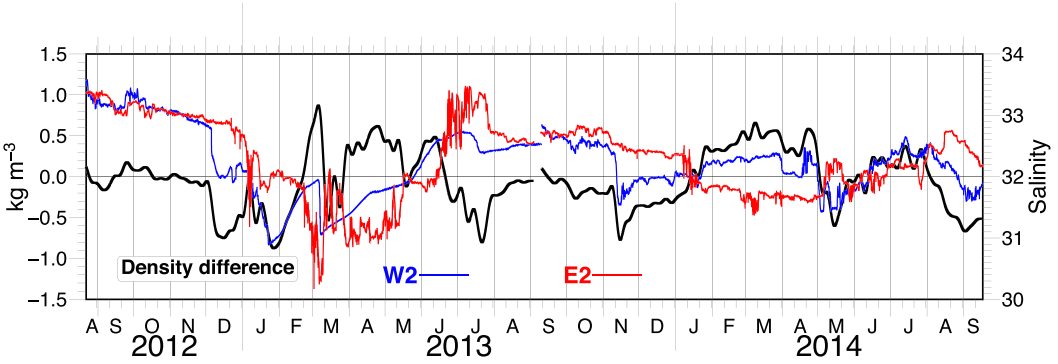

Figure 12. Near-bottom density difference (black) between W2 and E2, along with near-bottom salinities at W2 (blue) and E2 (red). Note that the near-bottom density difference is low-pass filtered to remove fluctuations at periods <8 days. Positive values indicate that the density at W2 is greater than that at E2.

across the northern Chukchi shelf. Some of this flow presumably merges with waters emanating from the Central Channel, although our results are ambiguous on this point. Clearly, the dense water that entered the Central Channel in the winter of 2012–2013 never appeared at W2. In addition, the bottom waters flowing past W2 in fall 2012 are cool (−1.0°C) and salty (33) while those in the Central Channel were ~1.0°C and 32. On the other hand, Weingartner, Fang, et al. (2017) found Central Channel waters in summer at the near surface in Region W. At best we conclude that there is a mixture of both Central Channel and western Chukchi shelf waters in this region, but more comprehensive measurements are required to determine the contributions from both sources.

The variation in bottom salinities between W2 and E2 imply the formation of along-isobath density gradients along the shelf north of Hanna Shoal. Such gradients, in conjunction with a cross-shelf bottom slope, can induce cross-shelf flows through divergence of bottom geostrophic currents (Csanady, 1985; Huthnance, 1984; Shaw & Csanady, 1988) and affect the vorticity balance by exerting a bottom pressure torque (Mertz, 1991). In both years the near-bottom density difference ($\Delta\rho_b$) between W2 and E2 varied substantially about zero (Figure 12, positive values imply greater density at W2 than at E2). In the 2012–2013 period, the record length average of $\Delta\rho_b$ was −0.07 kg m^{-3} and significantly different from zero, whereas in 2013–2014 the mean $\Delta\rho_b$ was not significantly different from zero. However, the magnitude of the deviations about the means can be much larger than the mean and the deviations tend to persist for a month or longer. Moreover, the data suggest that the gradient varies on a quasi-annual cycle. In late summer and early fall the difference was negligible, except in 2014. From late fall through early winter, the gradient is negative because of zonal differences in stratification; the less stratified waters at W2 erode and freshen the bottom layer earlier than the more stratified waters at E2. The gradient reverses sign in early winter as the fresh bottom waters at W2 flow eastward and are replaced by denser water. Simultaneously, the bottom waters at E2 are freshening due to vertical mixing and the gradual arrival of lower salinity waters from the west. The gradient switches sign again in spring and early summer as W2 freshens and the dense water from the western side of the Shoal arrives at E2. Consequently, the temporal variability in this gradient is a function of stratification differences (and the rate at which fall mixing proceeds) and the advection rate of different water masses from the west to the east.

Figure 13 is a circulation schematic that places our results in the context of previous findings. The regional circulation consists largely of barotropic flows on the Beaufort Sea shelf, in Barrow Canyon, and over the shelf south and west of Hanna Shoal (black arrows), with the latter involving a poorly observed eastward drift from Herald Valley and/or the western Chukchi Sea (dashed black arrow). Depending upon the wind strength, the westward drift over the Beaufort shelf will either join the along-canyon flow or cross the canyon onto the shelf east of Hanna Shoal (Okkonen et al., 2011; Weingartner, Danielson, et al., 2017; Weingartner, Potter, et al., 2017). On the north and east sides of Hanna Shoal the flow above ~30-m depth is northwestward (red arrow) and forced by persistently strong lateral salinity gradients. Below this depth the flow (yellow arrow) is southeastward and eventually spills into Barrow Canyon along its western rim. Over the slope, the deep, bottom-confined shelfbreak jet (green arrow, Corlett & Pickart, 2017) transports cold, saline

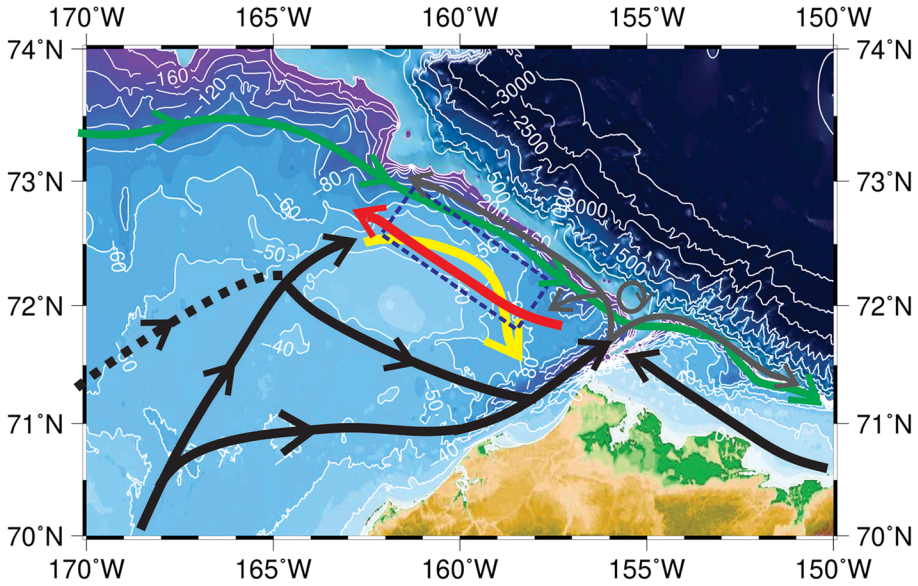

Figure 13. Schematic circulation of the northeast Chukchi Sea. Black arrows indicate vertically averaged flows, with the dashed black line implying a presumed pathway from the western Chukchi Sea. Red and yellow arrow indicate pathways for the upper and lower half of the water column, respectively, north and east of Hanna shoal. Gray arrows indicate possible pathways for Barrow Canyon outflow. The blue box denotes the region of along- and cross-shelf water mass exchange.

winter waters of Pacific origin from Herald Valley eastward along both the Chukchi and Beaufort seas. The Barrow Canyon outflow may have a number of different fates (gray arrows). Some of it may flow eastward along the Beaufort shelfbreak including dense waters that enter the shelfbreak jet and less dense, near-surface waters, flowing eastward above the jet. This surface flow gradually diminishes in strength as it breaks up via instabilities (von Appen & Pickart, 2011). Another portion of the canyon outflow may flow westward within the Chukchi Slope Current, above the shelfbreak jet (Corlett & Pickart, 2017). A third fate may be in the form of anticyclonic eddies generated at the canyon's mouth, which then propagate into the basin (D'Asaro, 1988a, D'Asaro, 1988b).

The shelf north of Hanna Shoal (dotted box) appears to be a region of active water exchange. These exchanges involve along-shelf transfers of generally saltier deeper waters entering from the western and/or central Chukchi shelf and more dilute surface waters derived from the shelfbreak, Barrow Canyon, and/or the Beaufort shelf. In addition, our results suggest that cross-shelf exchanges, mediated by along-isobath density gradients, may also occur here. Although we found no statistically significant correlation between the along- and cross-isobath velocity components and the density gradient, our representation of the along-shelf density gradient may be spatially biased insofar as we did not resolve the vertical or horizontal extent of the density differences (although the latter are likely smaller than the along-isobath spacing of the moorings). Consequently, it is impossible to quantify their effects on cross-shelf exchange and suggest that this be a topic for the future. The persistently strong stratification east of Hanna Shoal and the observations of Weingartner, Fang, et al. (2017) suggest that the along-isobath density gradient in the upper water column is generally positive. Thus, there may be times when the cross-shelf geostrophic component is vertically compensated and other times when the along-shelf flow must be divergent or convergent in order to maintain flow continuity. In either case these density gradients may result in substantial cross-shelf exchanges.

Data Availability Statement

NCEP Reanalysis data were obtained from the NOAA/OAR/ESRL PSD, Boulder, CO, USA, and are available at this website (http://www.esrl.noaa.gov/psd/). The ASL, COMIDA, and Barrow Canyon mooring data are available at NODC via https://www.nodc.noaa.gov/archive/arc0111/0164964/, https://www.nodc.noaa.gov/archive/arc0109/0163833/, and https://www.nodc.noaa.gov/archive/arc0113/0160090/, respectively.

Acknowledgments

This work was supported by Bureau of Ocean Energy Management (BOEM) Contract M11AC00007 (COMIDA) and Contracts M12AC000008 and M09AC15207 (Barrow Canyon). The ASL moorings were supported by ConocoPhillips Alaska Inc. (CPAI), Shell Exploration and Production, Inc. (SEPI), and Statoil USA Exploration and Production as part of the Chukchi Sea Environmental Studies Program (CSESP). We thank the officers and crews of the numerous vessels that deployed and recovered the moorings. Y.-C. Fang gratefully acknowledges Alfred Wegener Institute for providing resources and salary support in the preparation of the manuscript by Budget IP82100022. We are grateful for the fruitful discussions with B. Rabe, M. Janout, H. Hellmer, W.-J. von Appen, J. Schaffer, A. Münchow, C. Elmer, Y. Kawaguchi, and M. Barbat. Special thanks to B. Rabe for his continued support and encouragement in preparing this paper. We appreciate Projekt DEAL supporting open access of our paper. We sincerely thank the Editor, Laurence Padman, and one anonymous reviewer for their constructive reviews, which greatly improved the paper.

References

Aagaard, K., Coachman, L. K., & Carmack, E. (1981). On the halocline of the Arctic Ocean. *Deep Sea Research Part A. Oceanographic Research Papers*, *28*(6), 529–545. https://doi.org/10.1016/0198-0149(81)90115-1

Aagaard, K., & Roach, A. T. (1990). Arctic Ocean-shelf exchange: Measurements in Barrow Canyon. *Journal of Geophysical Research: Oceans*, *95*(C10), 18163. https://doi.org/10.1029/jc095ic10p18163

Aagaard, K., Weingartner, T. J., Danielson, S. L., Woodgate, R. A., Johnson, G. C., & Whitledge, T. E. (2006). Some controls on flow and salinity in Bering Strait. *Geophysical Research Letters*, *33*, L19602. https://doi.org/10.1029/2006GL026612

Auad, G., & Hendershott, M. C. (1997). The low-frequency transport in the Santa Barbara Channel: Description and forcing. *Continental Shelf Research*, *17*(7), 779–802. https://doi.org/10.1016/S0278-4343(96)00062-3

Barnett, T. P. (1983). Interaction of the monsoon and Pacific trade wind system at interannual time scales part I: The equatorial zone. *Monthly Weather Review*, *111*(4), 756–773. https://doi.org/10.1175/1520-0493(1983)111<0756:IOTMAP>2.0.CO;2

Beckers, J. M., & Rixen, M. (2003). EOF calculations and data filling from incomplete oceanographic datasets. *Journal of Atmospheric and Oceanic Technology*, *20*(12), 1839–1856. https://doi.org/10.1175/1520-0426(2003)020<1839:ECADFF>2.0.CO;2

Blanchard, A. L., Day, R. H., Gall, A. E., Aerts, L. A. M., Delarue, J., Dobbins, E. L., et al. (2017). Ecosystem variability in the offshore Northeastern Chukchi Sea. *Progress in Oceanography*, *159*, 130–153. https://doi.org/10.1016/j.pocean.2017.08.008

Cavalieri, D. J., Parkinson, C. L., Gloersen, P., & Zwally, H. J. (1996). *Updated yearly. sea ice concentrations from Nimbus-7 SMMR and DMSP SSM/I-SSMIS passive microwave data, version 1*. Boulder, CO: NASA National Snow and Ice Data Center Distributed Active Archive Center. https://doi.org/10.5067/8GQ8LZQVL0VL

Chavanne, C. P., Flament, P., Luther, D. S., & Gurgel, K.-W. (2010). Observations of vortex Rossby waves associated with a mesoscale cyclone*. *Journal of Physical Oceanography*, *40*, 2333–2340. https://doi.org/10.1175/2010JPO4495.1

Clarke, J. T., Moore, S. E., & Ljungblad, D. K. (1989). Observations on gray whale (Eschrichtius robustus) utilization patterns in the northeastern Chukchi Sea, July–October 1982–1987. *Canadian Journal of Zoology*, *67*(11), 2646–2654. https://doi.org/10.1139/z89-374

Coachman, L. K., Aagaard, K., & Tripp, R. B. (1975). *Bering Strait: The regional physical oceanography*. Seattle: University of Washington Press.

Corlett, W. B., & Pickart, R. S. (2017). The Chukchi slope current. *Progress in Oceanography*, *153*, 50–65. https://doi.org/10.1016/j.pocean.2017.04.005

Csanady, G. T. (1985). "Pycnobathic" currents over the upper continental slope. *Journal of Physical Oceanography*, *15*(3), 306–315. https://doi.org/10.1175/1520-0485(1985)015<0306:COTUCS>2.0.CO;2

Cushman-Roisin, B., & Beckers, J.-M. (2011). Chapter 9 - Barotropic waves. In B. Cushman-Roisin & J.-M. Beckers (Eds.), *Introduction to geophysical fluid dynamicsphysical and numerical aspects* (Vol. 101, pp. 271–315). Elsevier: Academic Press. https://doi.org/10.1016/B978-0-12-088759-0.00009-2

D'Asaro, E. A. (1988a). Generation of submesoscale vortices: A new mechanism. *Journal of Geophysical Research: Oceans*, *93*(C6), 6685–6693. https://doi.org/10.1029/JC093iC06p06685

D'Asaro, E. A. (1988b). Observations of small eddies in the Beaufort Sea. *Journal of Geophysical Research: Oceans*, *93*(C6), 6669–6684. https://doi.org/10.1029/JC093iC06p06669

Danielson, S. L., Eisner, L., Ladd, C., Mordy, C., Sousa, L., & Weingartner, T. J. (2017). A comparison between late summer 2012 and 2013 water masses, macronutrients, and phytoplankton standing crops in the northern Bering and Chukchi seas. *Deep Sea Research Part II: Topical Studies in Oceanography*, *135*, 7–26. https://doi.org/10.1016/j.dsr2.2016.05.024

Danielson, S. L., Weingartner, T. J., Hedstrom, K. S., Aagaard, K., Woodgate, R., Curchitser, E., & Stabeno, P. J. (2014). Coupled wind-forced controls of the Bering–Chukchi shelf circulation and the Bering Strait throughflow: Ekman transport, continental shelf waves, and variations of the Pacific–Arctic Sea surface height gradient. *Progress in Oceanography*, *125*, 40–61. https://doi.org/10.1016/j.pocean.2014.04.006

Emery, W. J., & Thomson, R. E. (1997). *Data analysis methods in physical oceanography*. UK: Pergamon.

Fang, Y.-C., Potter, R. A., Statscewich, H., Weingartner, T. J., Winsor, P., & Irving, B. K. (2017). Surface current patterns in the northeastern Chukchi Sea and their response to wind forcing. *Journal of Geophysical Research: Oceans*, *122*, 9530–9547. https://doi.org/10.1002/2017JC013121

Gawarkiewicz, G., & Chapman, D. C. (1995). A numerical study of dense water formation and transport on a shallow, sloping continental shelf. *Journal of Geophysical Research: Oceans*, *100*(C3), 4489–4507. https://doi.org/10.1029/94JC01742

Gong, D., & Pickart, R. S. (2015). Summertime circulation in the eastern Chukchi Sea. *Deep Sea Research Part II: Topical Studies in Oceanography*, *118*, 18–31. https://doi.org/10.1016/j.dsr2.2015.02.006

Grantz, A., and Eittreim, S. (1979). Geology and physiography of the continental margin north of Alaska and implications for the origin of the Canada basin, U.S. Geological Survey, Open File Report 79–288.

Grebmeier, J. M., Bluhm, B. A., Cooper, L. W., Danielson, S. L., Arrigo, K. R., Blanchard, A. L., et al. (2015). Ecosystem characteristics and processes facilitating persistent macrobenthic biomass hotspots and associated benthivory in the Pacific Arctic. *Progress in Oceanography*, *136*, 92–114. https://doi.org/10.1016/j.pocean.2015.05.006

Grebmeier, J. M., Cooper, L. W., Feder, H. M., & Sirenko, B. I. (2006). Ecosystem dynamics of the Pacific-influenced northern Bering and Chukchi seas in the Amerasian Arctic. *Progress in Oceanography*, *71*(2–4), 331–361. https://doi.org/10.1016/j.pocean.2006.10.001

Hirano, D., Fukamachi, Y., Watanabe, E., Ohshima, K. I., Iwamoto, K., Mahoney, A. R., et al. (2016). A wind-driven, hybrid latent and sensible heat coastal polynya off Barrow, Alaska. *Journal of Geophysical Research: Oceans*, *121*, 980–997. https://doi.org/10.1002/2015JC011318

Huthnance, J. M. (1984). Slope currents and "JEBAR.". *Journal of Physical Oceanography*, *14*(4), 795–810. https://doi.org/10.1175/1520-0485(1984)014<0795:SCA>2.0.CO;2

Itoh, M., Nishino, S., Kawaguchi, Y., & Kikuchi, T. (2013). Barrow canyon volume, heat, and freshwater fluxes revealed by long-term mooring observations between 2000 and 2008. *Journal of Geophysical Research: Oceans*, *118*, 4363–4379. https://doi.org/10.1002/jgrc.20290

Johnson, W. R. (1989). Current response to wind in the Chukchi Sea: A regional coastal upwelling event. *Journal of Geophysical Research: Oceans*, *94*(C2), 2057–2064. https://doi.org/10.1029/JC094iC02p02057

Kaihatu, J. M., Handler, R. A., Marmorino, G. O., & Shay, L. K. (1998). Empirical orthogonal function analysis of ocean surface currents using complex and real-vector methods. *Journal of Atmospheric and Oceanic Technology*, *15*(4), 927–941. https://doi.org/10.1175/1520-0426(1998)015<0927:EOFAOO>2.0.CO;2

Kulikov, E. A., Rabinovich, A. B., & Carmack, E. C. (2004). Barotropic and baroclinic tidal currents on the Mackenzie shelf break in the southeastern Beaufort Sea. *Journal of Geophysical Research: Oceans*, *109*, C05020. https://doi.org/10.1029/2003JC001986

Ladd, C., Mordy, C. W., Salo, S. A., & Stabeno, P. J. (2016). Winter water properties and the Chukchi Polynya. *Journal of Geophysical Research: Oceans*, *121*, 5516–5534. https://doi.org/10.1002/2016JC011918

Large, W. G., & Pond, S. (1981). Open ocean momentum flux measurements in moderate to strong winds. *Journal of Physical Oceanography*, *11*(3), 324–336. https://doi.org/10.1175/1520-0485(1981)011<0324:OOMFMI>2.0.CO;2

Li, M., Pickart, R. S., Spall, M. A., Weingartner, T. J., Lin, P., Moore, G. W. K., & Qi, Y. (2019). Circulation of the Chukchi Sea shelfbreak and slope from moored timeseries. *Progress in Oceanography*, *172*, 14–33. https://doi.org/10.1016/j.pocean.2019.01.002

Lin, P., Pickart, R. S., McRaven, L. T., Arrigo, K. R., Bahr, F., Lowry, K. E., et al. (2019). Water mass evolution and circulation of the northeastern Chukchi Sea in summer: Implications for nutrient distributions. *Journal of Geophysical Research: Oceans*, *124*, 4416–4432. https://doi.org/10.1029/2019JC015185

Lu, K., Weingartner, T., Danielson, S., Winsor, P., Dobbins, E., Martini, K., & Statscewich, H. (2015). Lateral mixing across ice meltwater fronts of the Chukchi Sea shelf. *Geophysical Research Letters*, *42*, 6754–6761. https://doi.org/10.1002/2015GL064967

Martin, S., & Drucker, R. (1997). The effect of possible Taylor columns on the summer ice retreat in the Chukchi Sea. *Journal of Geophysical Research*, *102*(C5), 10,410–10,473.

Mertz, G. (1991). The relationship of pycnobathic currents and baroclinic torques. *Journal of Physical Oceanography*, *21*(1), 181–183. https://doi.org/10.1175/1520-0485(1991)021<0181:TROPCA>2.0.CO;2

Mesinger, F., DiMego, G., Kalnay, E., Mitchell, K., Shafran, P. C., Ebisuzaki, W., et al. (2006). North American regional reanalysis. *Bulletin of the American Meteorological Society*, *87*, 343–360. https://doi.org/10.1175/BAMS-87-3-343

Miller, A. J., Lermusiaux, P. F. J., & Poulain, P.-M. (1996). A topographic–Rossby mode resonance over the Iceland–Faeroe ridge. *Journal of Physical Oceanography*, *26*(12), 2735–2747. https://doi.org/10.1175/1520-0485(1996)026<2735:ATMROT>2.0.CO;2

Moore, S. E., and Huntington, H. P. (2008). Arctic marine mammals and climate change: Impact and resilience. *Ecological Applications*, *18*(sp2), S157–S165. https://doi.org/10.1890/06-0571.1

Mountain, D. G., Coachman, L. K., & Aagaard, K. (1976). On the flow through Barrow canyon. *Journal of Physical Oceanography*, *6*(4), 461–470. https://doi.org/10.1175/1520-0485(1976)006<0461:OTFTBC>2.0.CO;2

Mudge, T. D., Fissel, D. B., Sadowy, D., Borg, K., Billeness, D., Knox, K., et al. (2015). Analysis of ice and Metocean measurements, Chukchi Sea 2013-2014, for Shell. Project Report for Shell International Exporation and Production Inc., Houston, Texas by ASL Environmental Sciences Inc., Victoria, B.C. Canada. Xi + 108p.

Nikolopoulos, A., Pickart, R. S., Fratantoni, P. S., Shimada, K., Torres, D. J., & Jones, E. P. (2009). The western Arctic boundary current at 152°W: Structure, variability, and transport. *Deep Sea Research Part II: Topical Studies in Oceanography*, *56*(17), 1164–1181. https://doi.org/10.1016/j.dsr2.2008.10.014

Okkonen, S. R., Ashjian, C. J., Campbell, R. G., Clarke, J. T., Moore, S. E., & Taylor, K. D. (2011). Satellite observations of circulation features associated with a bowhead whale feeding 'hotspot' near Barrow, Alaska. *Remote Sensing of Environment*, *115*, 2168–2174. https://doi.org/10.1016/j.rse.2011.04.024

Paquette, R. G., & Bourke, R. H. (1974). Observations on the coastal current of arctic Alaska. *Journal of Marine Research*, *32*, 195–207.

Parkinson, C. L., & Comiso, J. C. (2013). On the 2012 record low Arctic Sea ice cover: Combined impact of preconditioning and an August storm. *Geophysical Research Letters*, *40*, 1356–1361. https://doi.org/10.1002/grl.50349

Peacock, N. R., & Laxon, S. W. (2004). Sea surface height determination in the Arctic Ocean from ERS altimetry. *Journal of Geophysical Research*, *109*, C07001. https://doi.org/10.1029/2001JC001026

Pickart, R. S. (2004). Shelfbreak circulation in the Alaskan Beaufort Sea: Mean structure and variability. *Journal of Geophysical Research*, *109*, C04024. https://doi.org/10.1029/2003JC001912

Pickart, R. S., Moore, G. W. K., Mao, C., Bahr, F., Nobre, C., & Weingartner, T. J. (2016). Circulation of winter water on the Chukchi shelf in early summer. *Deep Sea Research Part II: Topical Studies in Oceanography*, *130*, 56–75. https://doi.org/10.1016/j.dsr2.2016.05.001

Pickart, R. S., Pratt, L. J., Torres, D. J., Whitledge, T. E., Proshutinsky, A. Y., Aagaard, K., et al. (2010). Evolution and dynamics of the flow through Herald Canyon in the western Chukchi Sea. *Deep Sea Research Part II: Topical Studies in Oceanography*, *57*(1–2), 5–26. https://doi.org/10.1016/j.dsr2.2009.08.002

Pickart, R. S., Spall, M. A., Moore, G. W. K., Weingartner, T. J., Woodgate, R. A., Aagaard, K., & Shimada, K. (2011). Upwelling in the Alaskan Beaufort Sea: Atmospheric forcing and local versus non-local response. *Progress in Oceanography*, *88*(1-4), 78–100. https://doi.org/10.1016/j.pocean.2010.11.005

Schonberg, S. V., Clarke, J. T., & Dunton, K. H. (2014). Distribution, abundance, biomass and diversity of benthic infauna in the Northeast Chukchi Sea, Alaska: Relation to environmental variables and marine mammals. *Deep Sea Research Part II: Topical Studies in Oceanography*, *102*(supplement C), 144–163. https://doi.org/10.1016/j.dsr2.2013.11.004

Shaw, P.-T., & Csanady, G. T. (1988). Topographic waves over the continental slope. *Journal of Physical Oceanography*, *18*(6), 813–822. https://doi.org/10.1175/1520-0485(1988)018<0813:TWOTCS>2.0.CO;2

Shimada, K., Itoh, M., Nishino, S., McLaughlin, F., Carmack, E., & Proshutinsky, A. (2005). Halocline structure in the Canada Basin of the Arctic Ocean. *Geophysical Research Letters*, *32*, L03605. https://doi.org/10.1029/2004GL021358

Shimada, K., Kamoshida, T., Itoh, M., Nishino, S., Carmack, E., McLaughlin, F., et al. (2006). Pacific Ocean inflow: Influence on catastrophic reduction of sea ice cover in the Arctic Ocean. *Geophysical Research Letters*, *33*, L08605. https://doi.org/10.1029/2005GL025624

Spall, M. A. (2007). Circulation and water mass transformation in a model of the Chukchi Sea. *Journal of Geophysical Research*, *112*, C05025. https://doi.org/10.1029/2005JC003364

Stabeno, P., Kachel, N., Ladd, C., & Woodgate, R. (2018). Flow patterns in the eastern Chukchi Sea: 2010–2015. *Journal of Geophysical Research: Oceans*, *123*, 1177–1195. https://doi.org/10.1002/2017JC013135

Stigebrandt, A. (1984). The North Pacific: A global-scale estuary. *Journal of Physical Oceanography*, *14*(2), 464–470. https://doi.org/10.1175/1520-0485(1984)014<0464:TNPAGS>2.0.CO;2

von Appen, W.-J., & Pickart, R. S. (2011). Two configurations of the Western Arctic shelfbreak current in summer. *Journal of Physical Oceanography*, *42*, 329–351. https://doi.org/10.1175/JPO-D-11-026.1

Weingartner, T. J., Aagaard, K., Woodgate, R., Danielson, S., Sasaki, Y., & Cavalieri, D. (2005). Circulation on the north Central Chukchi Sea shelf. *Deep Sea Research Part II: Topical Studies in Oceanography*, *52*, 3150–3174. https://doi.org/10.1016/j.dsr2.2005.10.015

Weingartner, T. J., Cavalieri, D. J., Aagaard, K., & Sasaki, Y. (1998). Circulation, dense water formation, and outflow on the northeast Chukchi shelf. *Journal of Geophysical Research*, *103*(C4), 7647–7661. https://doi.org/10.1029/98JC00374

Weingartner, T. J., Danielson, S. L., Potter, R. A., Trefry, J. H., Mahoney, A., Savoie, M., et al. (2017). Circulation and water properties in the landfast ice zone of the Alaskan Beaufort Sea. *Continental Shelf Research*, *148*, 185–198. https://doi.org/10.1016/j.csr.2017.09.001

Weingartner, T. J., Dobbins, E., Danielson, S., Winsor, P., Potter, R., & Statscewich, H. (2013). Hydrographic variability over the northeastern Chukchi Sea shelf in summer-fall 2008–2010. *Continental Shelf Research*, *67*, 5–22. https://doi.org/10.1016/j.csr.2013.03.012

Weingartner, T. J., Fang, Y.-C., and Winsor, P. (2016). Physical oceanography and circulation. Chukchi Sea offshore monitoring in drilling area (COMIDA): Hanna Shoal ecosystem study final report, K. H. Dunton (Ed.).

Weingartner, T. J., Fang, Y.-C., Winsor, P., Dobbins, E., Potter, R., Statscewich, H., et al. (2017). The summer hydrographic structure of the Hanna Shoal region on the northeastern Chukchi Sea shelf: 2011–2013. *Deep Sea Research Part II: Topical Studies in Oceanography*, *144*, 6–20. https://doi.org/10.1016/j.dsr2.2017.08.006

Weingartner, T. J., Potter, R. A., Stoudt, C. A., Dobbins, E. L., Statscewich, H., Winsor, P. R., et al. (2017). Transport and thermohaline variability in Barrow Canyon on the Northeastern Chukchi Sea Shelf. *Journal of Geophysical Research: Oceans*, *122*, 3565–3585. https://doi.org/10.1002/2016JC012636

Weingartner, T. J., Winsor, P., Potter, R. A., Statscewich, H., and Dobbins, E. L. (2013). OCS study BOEM 2012-079 application of high frequency radar to potential hydrocarbon development areas in the Northeast Chukchi Sea. *Final Rep., U.S. Dept. of the Interior, Alaska Outer Continental Shelf Region Contract M09AC15207, OCS Study BOEM 2012-079, 162 Pp. [Available Online at* Www.Boem.Gov/ESPIS/5/5266.Pdf*]*.

Winsor, P., & Chapman, D. C. (2004). Pathways of Pacific water across the Chukchi Sea: A numerical model study. *Journal of Geophysical Research*, *109*, C03002. https://doi.org/10.1029/2003JC001962

Wood, K. R., Bond, N. A., Danielson, S. L., Overland, J. E., Salo, S. A., Stabeno, P. J., & Whitefield, J. (2015). A decade of environmental change in the Pacific Arctic region. *Progress in Oceanography*, *136*, 12–31. https://doi.org/10.1016/j.pocean.2015.05.005

Woodgate, R. A. (2018). Increases in the Pacific inflow to the Arctic from 1990 to 2015, and insights into seasonal trends and driving mechanisms from year-round Bering Strait mooring data. *Progress in Oceanography*, *160*(December 2017), 124–154. https://doi.org/10.1016/j.pocean.2017.12.007

Woodgate, R. A., Aagaard, K., & Weingartner, T. J. (2005). A year in the physical oceanography of the Chukchi Sea: Moored measurements from autumn 1990–1991. *Deep Sea Research Part II: Topical Studies in Oceanography*, *52*, 3116–3149. https://doi.org/10.1016/j.dsr2.2005.10.016

Woodgate, R. A., Weingartner, T. J., & Lindsay, R. (2010). The 2007 Bering Strait oceanic heat flux and anomalous Arctic Sea-ice retreat. *Geophysical Research Letters*, *37*, L01602. https://doi.org/10.1029/2009GL041621

Woodgate, R. A., Weingartner, T. J., & Lindsay, R. (2012). Observed increases in Bering Strait oceanic fluxes from the Pacific to the Arctic from 2001 to 2011 and their impacts on the Arctic Ocean water column. *Geophysical Research Letters*, *39*, L24603. https://doi.org/10.1029/2012GL054092

Yankovsky, A. E., & Chapman, D. C. (1995). Generation of mesoscale flows over the shelf and slope by shelf wave scattering in the presence of a stable, sheared mean current. *Journal of Geophysical Research*, *100*(C4), 6725–6742. https://doi.org/10.1029/94JC03339